Supplementary information

for

Porous noria polymer: a cage-to-network approach toward a robust catalyst for CO$_2$ fixation and nitroarene reduction

Arkaprabha Giri,‡ Niraj Nitish Patil,‡ and Abhijit Patra*

Department of Chemistry, Indian Institute of Science Education and Research Bhopal (IISERB),
Bhopal-462066, Fax: +91 (0)755 409 2392; Tel: +91 (0)755 669 1337
E-mail: abhijit@iiserb.ac.in

1. Instrumentation and chemicals

Nuclear magnetic resonance (NMR) spectroscopy: ^{1}H NMR spectroscopic analyses were carried out using Bruker Avance III 500 NMR spectrometer. The solid-state ^{13}C cross-polarization magic angle spinning (CP/MAS) NMR experiments were carried out on JEOL ECX2 400 MHz (field 9.4 T) using a 4 mm solid-state MAS probe. A 4 mm Zirconia rotor was used for packing the samples, and it was spun at 8 kHz at the magic angle.

Fourier transform infrared (FTIR) spectroscopy: Potassium bromide pellets were used to carry out FTIR measurements on Perkin-Elmer Model 2000 FTIR spectrometer. The represented data were the signal-averaged values of twenty scans at ambient conditions with a resolution of 4 cm^{-1}.

Thermogravimetric analysis (TGA): TGA measurements were performed on a Perkin Elmer TGA-6000 instrument. The samples were heated under a nitrogen atmosphere from 30 °C to 900 °C at a rate of 10 °C min^{-1}.

Powder X-ray diffraction (PXRD): PXRD experiments were conducted on a PANalytical Empyrean XRD instrument. Data were acquired for 2θ values of 5° to 80°.

Specific Brunauer–Emmett–Teller (BET) surface area analysis: All the nitrogen sorption measurements were carried out on Quantachrome Autosorb, QUA211011 equipment. Before analysis, the samples were degassed under a vacuum for 12 h at 80 °C. BET isotherms were analyzed using ASiQwin software.

Field emission scanning electron microscopy (FESEM): The morphology of the network polymer was investigated using Carl Zeiss (Ultraplus) field emission scanning electron microscope. FESEM samples were prepared by sprinkling ~ 0.5 mg of polymer on a carbon tape attached with an aluminium stub. Then the samples were coated with a thin layer of sputtered gold. The imaging was performed at an accelerating voltage of 5 kV and 20 kV.

High-resolution transmission electron microscopy (HRTEM): The morphology of the samples was examined through the FEI TALOS 200S instrument at a working voltage of 200 kV. The samples were prepared by drop-casting the supernatant of polymer dispersion in methanol on a lacey-carbon grid.

X-ray photoelectron spectroscopy (XPS): The XPS experiment was performed using PHI 5000 Versa Prob II, FIE Inc. For the measurement, a vacuum-dried powder sample drop was taken on a sample holder of the size 1.5 mm radius. The scan time was set for 1 h per element for the core level scan (energy band: 20 eV) with a pass setting of 23.5 eV. 0.025 eV step and 100 ms time per step for 5 cycles.

Steady-state UV-visible absorption spectroscopy: Cary 100 spectrophotometer was used to record the UV-visible spectra.

Inductively coupled plasma optical emission spectrometry (ICP-OES): Pristine and recycled Ag@NPOP were subjected to ICP-OES analysis to quantify the metal loading. 5 mg of Ag@NPOP was digested in aqua regia (diluted to 15 mL by water) and was analyzed for the amount of Ag present.

Chemicals: All chemicals were used as received unless stated otherwise. Glutaraldehyde aqueous solution (50% v/v), K_2CO_3 (>99%), tetrafluoroterephthalonitrile (99%), dimethylformamide (99.9%), sodium borohydride, silver nitrate, n-tetrabutylammonium bromide were purchased from Sigma-Aldrich. Resorcinol (98%) was received from Spectrochem.

2. Synthesis and characterization of noria cage
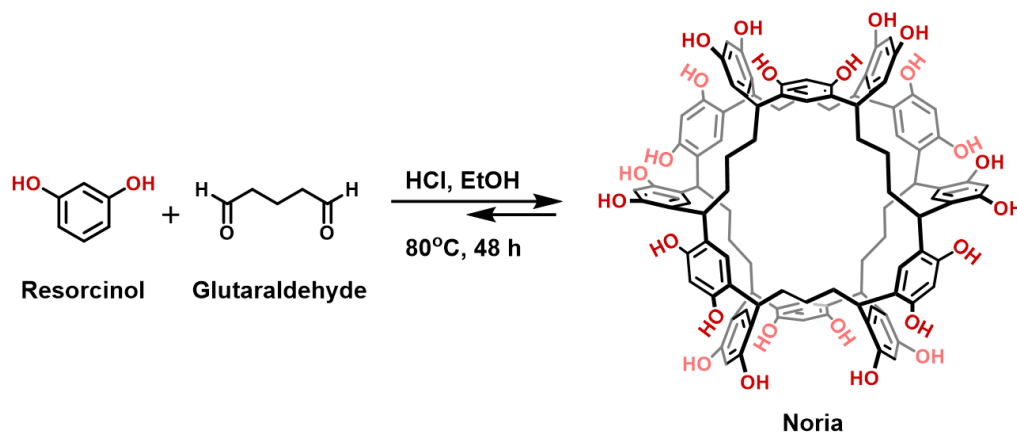
Scheme. S1 Synthetic scheme for noria.

We followed a reported procedure for the synthesis of the noria cage with minor modifications (Scheme S1).[1] Resorcinol (40 mmol, 4.4 g) and glutaraldehyde solution (50 wt. % in water, 8.0 mmol) were taken in a 250 mL round bottom flask and were dissolved in 50 mL of ethanol. Then 10 mL conc. HCl was added drop-wise with stirring at 2-3 ℃ for 30 min. The solution was further kept for stirring at 80 ℃ for 48 h. After that, the reaction mixture was cooled to room temperature. Then it was poured into 150 mL of cold methanol. The precipitate was collected by centrifugation and washed multiple times with water, methanol, and diethyl ether, and a pale-yellow color solid was obtained. The product was dried in a glass oven under vacuum for 24 h at 80 °C (Yield: ∼ 30 %). ^{1}H NMR (500 MHz, [D$_6$] DMSO, δ_H (ppm)): 0.81–2.90 (m, 36 H, -CH$_2$CH$_2$CH$_2$-), 3.88–4.32 (m, 12 H, CH), 6.0–6.3 (m, 12, Ar-H), 6.9-7.5 (m, 12 H, Ar-H), 8.65–9.45 (m, 24 H, OH, Fig. S25); ^{13}C NMR (126 MHz, [D$_6$] DMSO) δ_C (ppm)): 151.36, 151.31, 124.60, 122.66, 103.23, 102.33, 35.44, 33.64, 15.07 (Fig. S26). MALDI-TOF-MS: m/z [M]$^+$ calc. for (C$_{102}$H$_{96}$O$_{24}$):1704.63, found: 1704.10; calc. for (C$_{102}$H$_{96}$O$_{24}$+Na): 1727.86, found: 1727.06; calc. for (C$_{102}$H$_{96}$O$_{24}$+K): 1743.73, found: 1743.09.

3. Cage/cavitand-to-network design strategy

Nonporous monomers are mostly used as building blocks for the development of porous organic polymers (POPs). However, in recent years, an alternative strategy has emerged where three-dimensional 'preporous' building blocks, such as cavitands and cages with well-defined discrete cavities, or voids are employed for the development of a new generation of POPs (Fig. S1, Table S1).[2-9] In this approach, cage/ cavitand molecules are linked with different types of rigid aromatic linkers to form extended networks

with facile inter-pore connectivity. The benefit of the cage-to-network strategy is integrating the structural and functional properties (e.g., guest recognition) of the preporous building blocks into the final network.
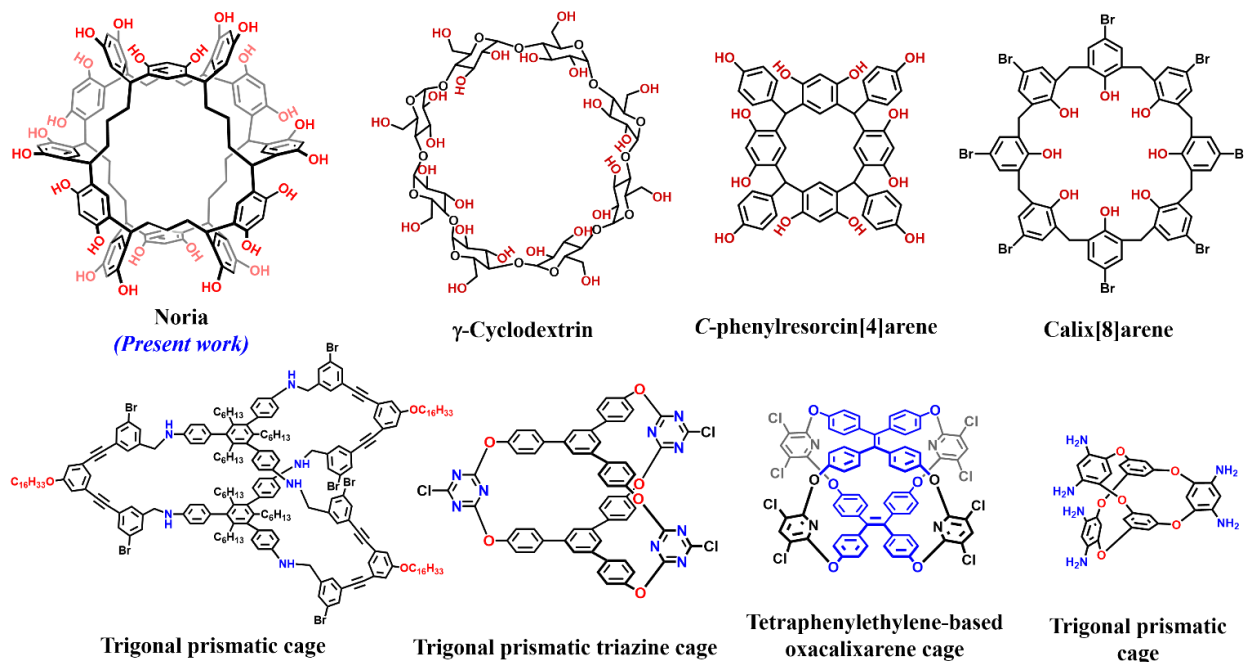

Fig. S1 The preporous cavitands and cages used for the development of porous organic polymers for multifarious applications.

Table S1. Preporous cavitand and cage-based building blocks with multiple propagating sites (cavitand $\geq$ 8, cage $\geq$ 3) used for the development of porous organic polymers.

Cavitand/Cage-based building block	Topology	Propa gating sites	Cage/ Cavitand-POPs (S_{BET}: m² g⁻¹)	Application	Reference
Noria cage	Water wheel structure	24	773	Selective CO_2 sorption, CO_2 conversion to cyclic carbonates, nitroarene reduction	*Present work*
γ-Cyclodextrin	Toroidal	24	934	Li-ion storage	*Angew. Chem. Int. Ed.,* 2017, **56,** 16313.[3]
C-phenyl resorcin[4]arene	Bucket	12	1225	CO_2 conversion to cyclic carbonates, size-charge selective molecular separation, gas sorption	*Chem. Mater.,* 2019, **31,** 8440.[4]
Calix[8]arene	Chalice	8	635	Removal of toxic herbicide paraquat from water	*J. Mater. Chem. A,* 2020, **8,** 13942.[5]
Trigonal prismatic cage	Trigonal prismatic	6	-	Selective CO_2 sorption	*Chem. Sci.,* 2012, **3,** 874.[6]
Trigonal prismatic triazine cage	Trigonal prismatic	3	844	Selective CO_2 sorption	*Chem. Mater.,* 2015, **27,** 4149.[7]
Tetraphenylethylene-based oxacalixarene cage	Quadr-angular prismatic	8	929	Selective CO_2 sorption and sensing	*Adv. Sci.,* 2018, **5,** 1800141.[8]

3.1 Fabrication of noria-based porous organic polymer (NPOP)

Noria cage has 24 phenolic hydroxyl groups. Therefore, we varied the linker (tetrafluoroterephthalonitrile, TFN) to noria ratio from 3 to 12 to knit noria (Table S2). We optimized the fabrication conditions by varying solvents and the equivalent of the base (Table S2). We found a lower surface area of the polymer by using three equivalents of TFN. This might be due to the lower degree of crosslinking. On the other hand, we observed that a higher equivalent of crosslinkers (TFN, 12 equiv.) led to the formation of soluble nonporous oligomers, which might be due to the steric factor associated with bulky noria cage. We got the highest surface area of the polymer with better yield by employing 6 equivalent of TFN. Furthermore, solvent optimization provided the highest surface area materials. The optimized reaction conditions are discussed provided below and are represented in Table S2.

Noria (100 mg, 0.06 mmol) and tetrafluoroterephthalonitrile (TFN, 72 mg, 6 equiv., 0.35 mmol) were added to a 15 mL sealed-Schlenk tube (Table S2). 5 mL 1:1 (v/v) mixture of anhydrous DMF and 1,4-dioxane were charged to Schlenk tube. The mixture was warmed to dissolve the monomers. The mixture was brought to room temperature, and finely ground K_2CO_3 (215 mg, 1.56 mmol) was added to it. The reaction mixture was degassed by three consecutive freeze-pump-thaw cycles. Then the reaction mixture was stirred at 85 °C for 48 h under a nitrogen atmosphere. It was allowed to cool to room temperature and quenched with 1 M HCl solution (10 mL). The precipitate was separated using centrifugation and washed with 1,4-dioxane, methanol, and diethyl ether. Next, it was thoroughly washed by Soxhlet extraction for 24 h each in THF, methanol, and chloroform, respectively. The resulting brown solid was dried under vacuum at 120 °C to yield NPOP polymer (estimated yield ∼ 60 %, considering 1:6 ratio of noria and TFN in the repeating unit).

Table S2: Optimization table for the synthesis of NPOP.

Entry	Noria (Equiv.)	TFN (Equiv.)	K_2CO_3 (Equiv.)	Temp. (°C)	Solvent	Remarks
1	1	3	12	120 (48 h)	DMSO	Surface area (<100 m^2 g^{-1})
2	1	6	12	120 (48 h)	DMSO	
3	1	12	26	120 (48 h)	DMSO	Formation of oligomer soluble in DMSO, DMF (nonporous)
4	1	6	26	85 (48 h)	DMF	Surface area (597 m^2 g^{-1})
5	1	6	26	85 (48 h)	DMF/Dioxane (1:1)	Surface area (720-773 m^2 g^{-1})

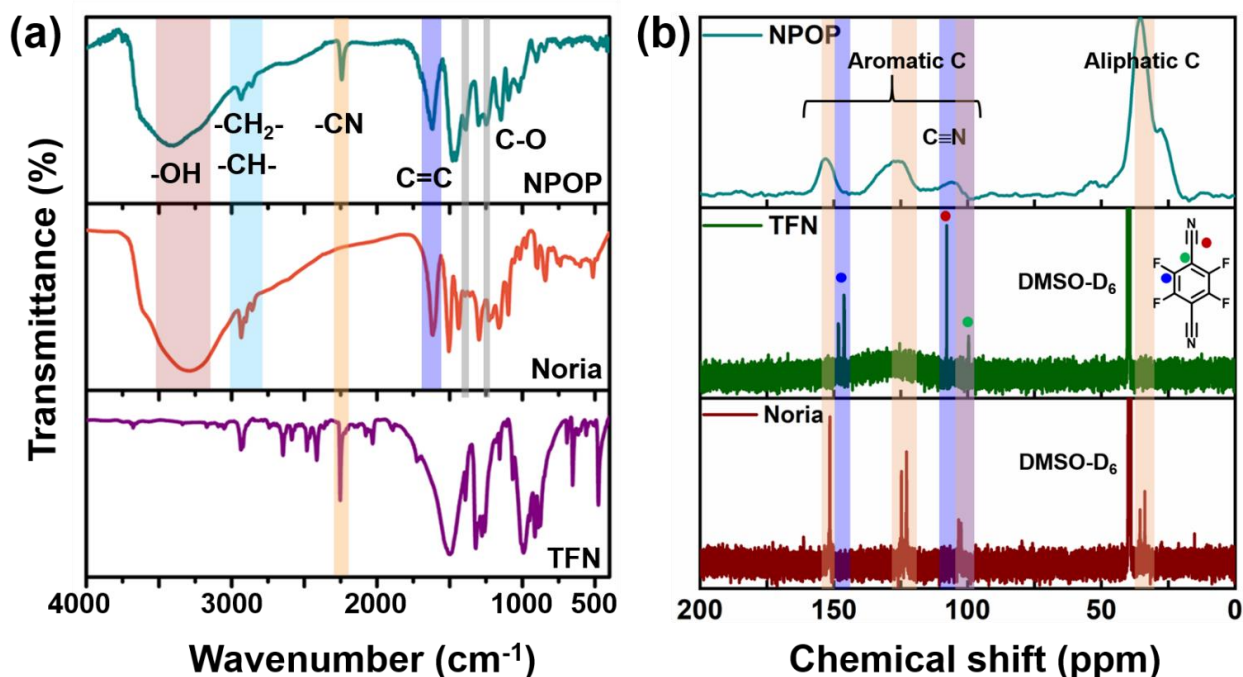## 3.2 FTIR and Solid-state ^{13}C (CP/MAS) NMR analysis

Fig. S2 (a) FTIR spectra of NPOP compared with noria and tetrafluoroterephthalonitrile (TFN). (b) ^{13}C NMR spectra of noria, tetrafluoroterephthalonitrile (TFN) in DMSO-D$_6$, and ^{13}C (CP/MAS) solid-state NMR spectrum of NPOP (bottom to top). The chemically nonequivalent C-atoms in TFN are designated by red, green, and blue-filled circles (middle panel).

We performed a comparative FTIR analysis employing NPOP, noria cage and crosslinker tetrafluoroterephthalonitrile (TFN, Fig. S2a). The peaks at 1094 and 1248 cm^{-1} suggested the C−O−C bond formation during S$_N$Ar reaction. We compared the solid-state ^{13}C cross-polarization magic angle spinning (CP/MAS) NMR of NPOP with solution-state ^{13}C NMR of pristine noria cage and TFN in D$_6$-DMSO (Fig. S2b). In the solid-state ^{13}C (CP/MAS) NMR, we observed sharp peaks at 28 and 35 ppm that were attributed to the –CH– and –CH$_2$– functionalities present in the noria core, respectively. Whereas peak resonating around 153 ppm was indicative of the formation of aryl C-O bonds.[10] The peak resonating around 105 ppm in the solid-state ^{13}C NMR of NPOP is due to the C-atoms of the nitrile group (C≡N) present in the TFN linker.[10] Broad peaks from 115 to 140 ppm were attributed to the aromatic carbons present in the noria and TFN moieties.

3.3 Thermogravimetric analysis (TGA)

The thermogravimetric analysis of NPOP revealed that the POP was stable up to ~ 400 °C (Fig. S3). 3-5 % mass loss at around 100°C was attributed to the evaporation of the trapped solvent molecules.
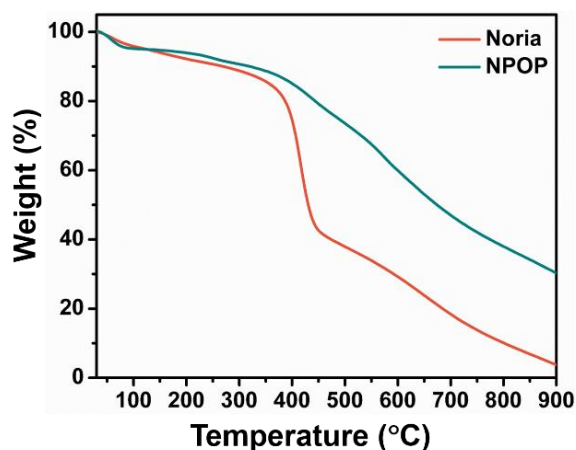
Fig. S3 Thermogravimetric analysis of noria and NPOP.

3.4 Surface area and pore size distribution analysis

The specific surface area and pore size distributions were estimated by N_2 adsorption-desorption isotherms at 77 K. The pore size distributions of the pristine noria and POPs were obtained through the non-local density functional theory method (NLDFT, carbon, slit pore, equilibrium model).[11] The specific surface areas were obtained by fitting the adsorption isotherm with Brünauer–Emmett–Teller (BET) equation as given below (Eq. 1).[11]

$$\frac{P/P_0}{n(1-\frac{P}{P_0})} = \frac{1}{n_m C} + \frac{C-1}{n_m C}\left(\frac{P}{P_0}\right) \qquad (1)$$

Where P/P_0 is the relative pressure, n is the specific amount adsorbed at P/P_0, n_m is the specific monolayer capacity, and C is the BET constant. The specific Brünauer–Emmett–Teller (BET) surface area of noria and NPOP were determined to be 218 ± 3 $m^2\,g^{-1}$, 748 ± 25 $m^2\,g^{-1}$, respectively (Fig. S4). Noria displayed a Type II isotherm, while NPOP exhibited Type Ib isotherm with H4 type hysteresis loop.[11] An H4 type hysteresis loop suggested the presence of narrow mesopores (2-5 nm). The t-plot method was employed
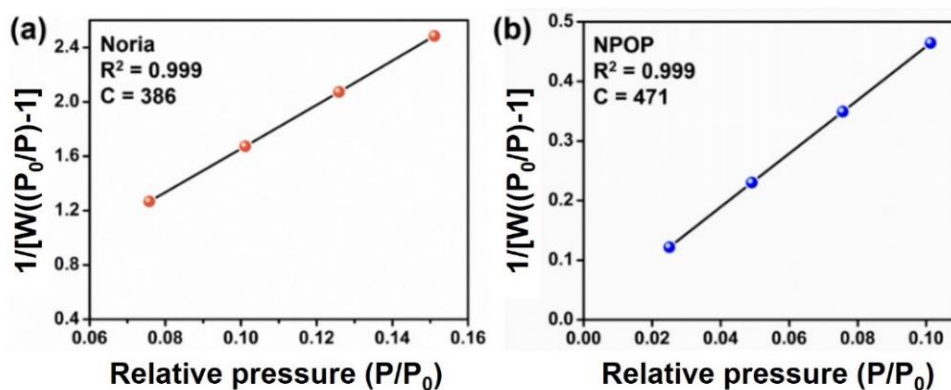

Fig. S4 Specific BET surface area plots for (a) noria and (b) NPOP.

using carbon-black as a standard to calculate the micropore volume (V_{micro}), micropore area (S_{micro}), and the total pore volume (V_{tot}) at relative pressure (P/P$_0$) of 0.95 (Table S3).

Table S3 Summary of the gas adsorption properties of different batches of noria and NPOP.

Entry	S_{BET} (m^2 g^{-1})	Avg. S_{BET} (m^2 g^{-1})	S_{micro} (m^2 g^{-1})	V_{micro} (cm^3 g^{-1})	V_{tot} (cm^3 g^{-1})
Noria	215 (1st batch), 221 (2nd batch)	218 ± 3	103	0.05	0.24
NPOP	773 (1st batch), 720 (2nd batch)	748 ± 25	502	0.22	0.49

In order to understand the role of the noria cage, we synthesized an analogous polymer of NPOP, Ph-POP, employing a flat aromatic phenolic core, phloroglucinol, and TFN (1: 3 ratio). The specific surface area of Ph-POP was found to be only 15 m^2 g^{-1} (Fig. S5a). The non-porous nature of Ph-POP compared to the high surface area and microporous nature of NPOP ascertained the importance of the 'cage-to-network' strategy applying noria as the building unit.
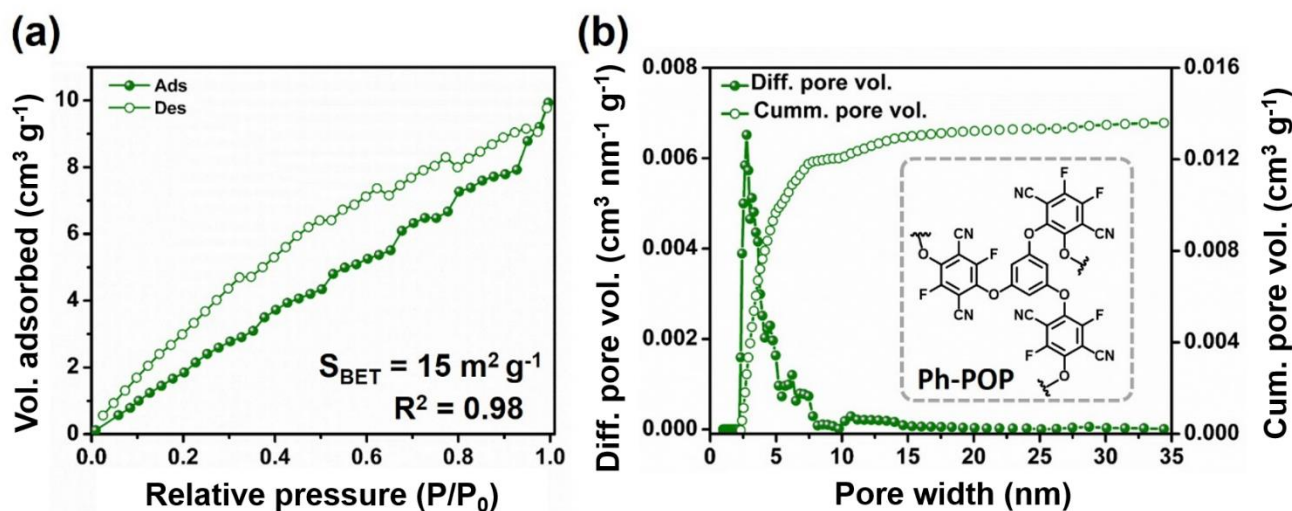

Fig. S5 (a) Nitrogen sorption isotherms and (b) NLDFT pore size distribution plots for Ph-POP (polymers without noria cage).

3.5 Morphological analysis

Morphological analyses were carried out using a field emission scanning electron microscope (FESEM) and a high-resolution transmission electron microscope (HRTEM). FESEM images revealed plate-like morphology for NPOP polymer. The HRTEM images of NPOP showed the porous structure typically observed in the amorphous POPs (Fig. S6).[12]
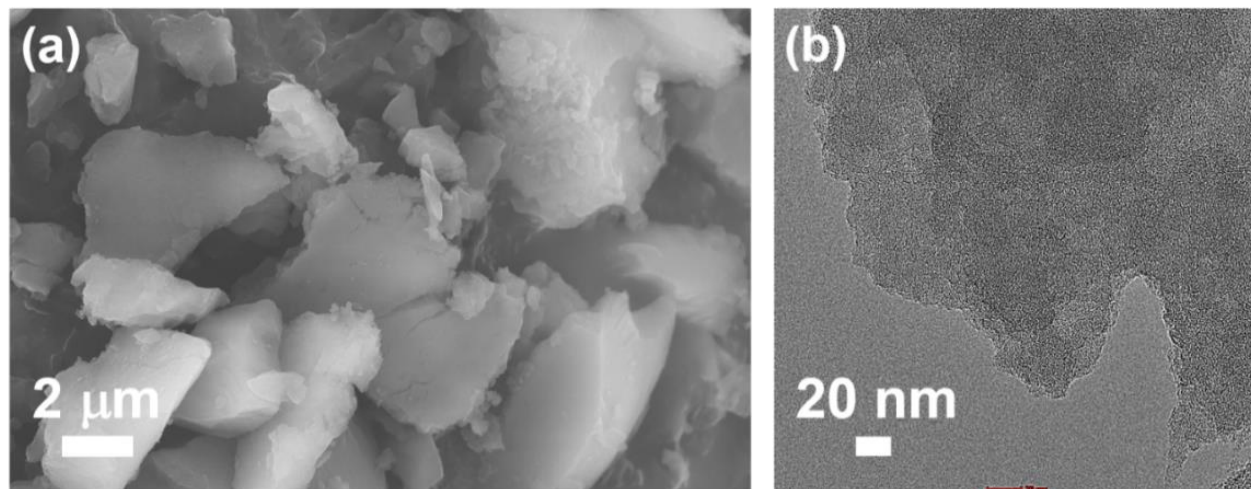

Fig. S6 (a) FESEM and (b) HRTEM images of NPOP.

3.6 Powder X-ray diffraction analysis

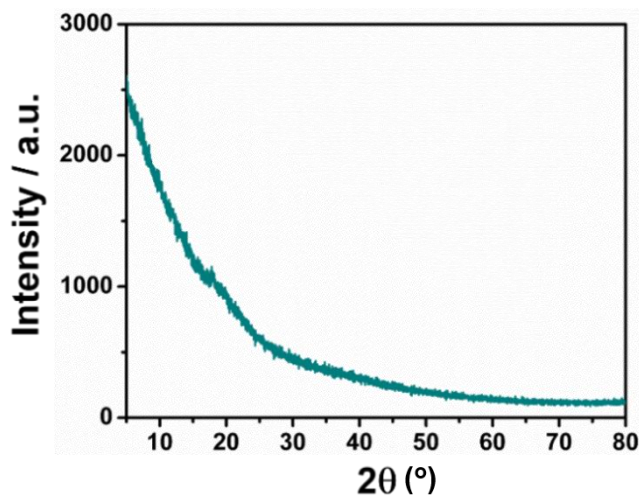Powder X-ray diffraction (PXRD) analysis of NPOP confirmed the amorphous nature of the polymer (Fig. S7).

Fig. S7 Powder X-ray diffraction analysis of NPOP.

4. Selective CO$_2$ adsorption

The CO$_2$ sorption isotherms of the noria and NPOP were measured at 273 K as well as 298 K (Fig. S8). A flue gas composition of 15% CO$_2$ and 85% N$_2$ was considered according to ideal adsorbed solution theory (IAST) for the calculation of CO$_2$ over N$_2$ selectivity (Eq. 2).[13]

$$Selectivity = \frac{q_1/q_2}{P_1/P_2} \qquad (2)$$

Where q$_1$ and q$_2$ are the amounts of adsorbate at pressure P$_1$ and P$_2$, respectively. The CO$_2$/N$_2$ selectivity of noria and NPOP at 273 K were found to be 24 and 30, respectively.

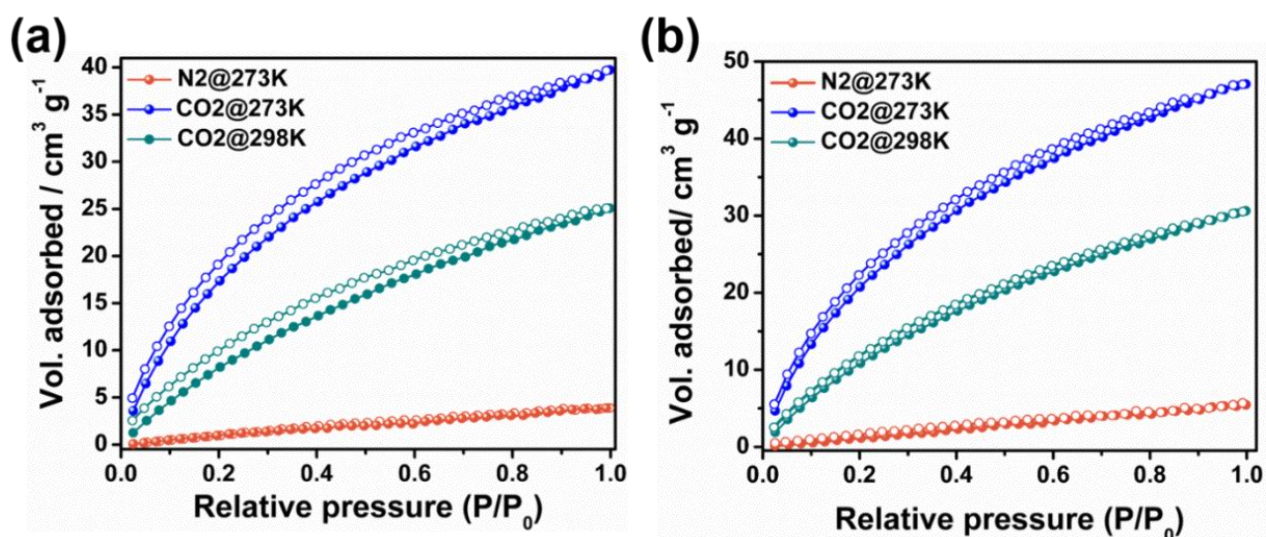**Fig. S8.** CO$_2$ sorption isotherms at 273 K and 298 K and N$_2$ sorption isotherms at 273 K of (a) noria and (b) NPOP (filled circle: adsorption, hollow circle: desorption).

The isosteric heat of adsorption (Q_{st}) for CO$_2$ was calculated from the adsorption isotherms measured at 273 K and 298 K considering the fixed amount of adsorbate using the Clausius-Clapeyron equation (Eq. 3).[13]

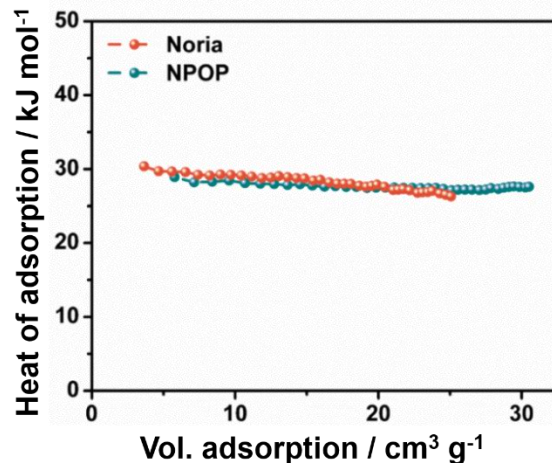$$\ln\left(\frac{P_1}{P_2}\right) = \frac{H_{abs}}{T}\left(\frac{1}{T_2} - \frac{1}{T_1}\right) \qquad (3)$$

Fig. S9 The isosteric heat of adsorption (Q_{st}) profiles of noria and NPOP.

Where P_1 and P_2 are the pressure for the same volume of the gas adsorbed at two different temperatures, T_1 and T_2, respectively. ΔH_{ads} (or, Q_{st}) gives the isosteric heat of adsorption (Fig. S9). The heat of adsorption for noria and NPOP were found to be almost similar, 30.4 and 28.9 kJ mol^{-1}, respectively. The high heat of adsorption was attributed to the facile interaction of CO_2 with the heteroatom-rich porous network as well as the 'cage-effect' associated with the noria core.[7]

5. Chemical fixation of CO₂

5.1. Catalytic conversion of epoxides and CO₂ to cyclic carbonates

The catalytic fixation of carbon dioxide to cyclic organic carbonates has attracted significant attention because of the use of cyclic carbonates as electrolytes for Li-ion batteries, polar aprotic solvents, fuel additives, etc. The reaction was optimized by taking styrene oxide (10 mmol) as the model substrate due to its high boiling point. The reaction was performed at 2.5 bar of carbon dioxide pressure at 90 °C using NPOP (30 mg, 0.14 mol %) as a catalyst and tetra-n-butyl ammonium bromide (TBAB, 0.30 mmol, 2.9 mol %) as cocatalyst under solvent-free conditions for 12 h (Scheme S2).
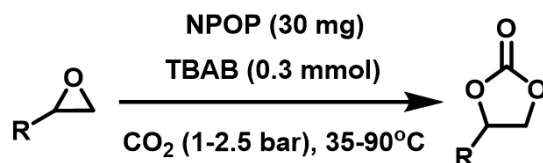
Scheme S2 Schematic illustration for the reaction conditions of the catalytic conversion of carbon dioxide and epoxides to cyclic carbonates using NPOP.

The H-bonding interaction between phenolic -OH and epoxide oxygen activates the substrate.[4,14] Subsequently, the nucleophile Br- from the cocatalyst TBAB attacks the sterically less hindered carbon of the epoxide leading to the ring-opening. This step is defined as the rate-determining step of the reaction. The resultant oxoanion attacks the carbon atom of CO₂, which is entrapped into the N and O-rich porous network due to the favorable ion-quadrupole interactions (as indicated by the high heat of CO₂ adsorption for NPOP: 28.9 kJ mol⁻¹).[13] It leads to an intermediate carbonate formation. At the end, the intramolecular ring closure results in the desired cyclic carbonate as a product with the recovery of TBAB (Fig. S10).
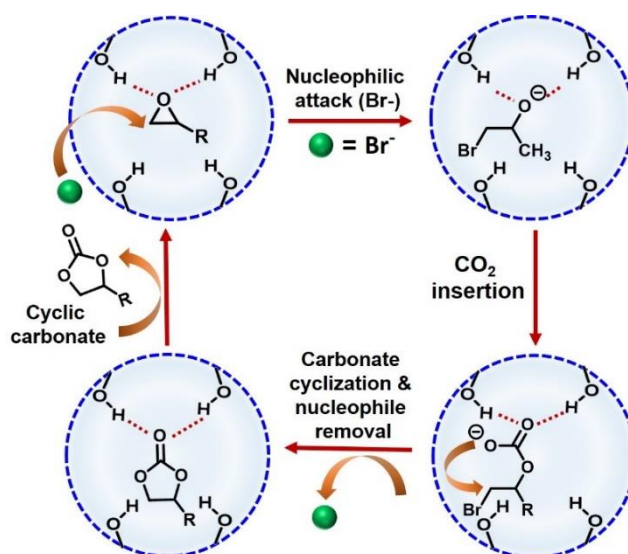

Fig. S10 A plausible mechanism for the chemical fixation of CO₂ and epoxide to cyclic organic carbonate by noria and noria-based porous organic polymer (NPOP).

The turnover number of the catalysts (TON = number of moles of reactant consumed/mole of catalyst) was calculated considering the catalytically active sites, i.e., noria unit. We found the turnover numbers for noria and NPOP were 477 and 511, respectively.

5.2 Recyclability

The catalyst was recovered by centrifuging the reaction mixture and was regenerated by washing with dichloromethane and kept for drying under vacuum at 100 °C in the oven for 12 h. The catalyst was highly effective for 10 consecutive cycles. The slight reduction in % of conversion was mostly due to the loss of the catalyst during the workup. The % of conversion was found to be unchanged if we maintain the catalyst amount identical circumventing the weight loss in subsequent cycles (~1 mg/cycle) (Fig. S11a). The
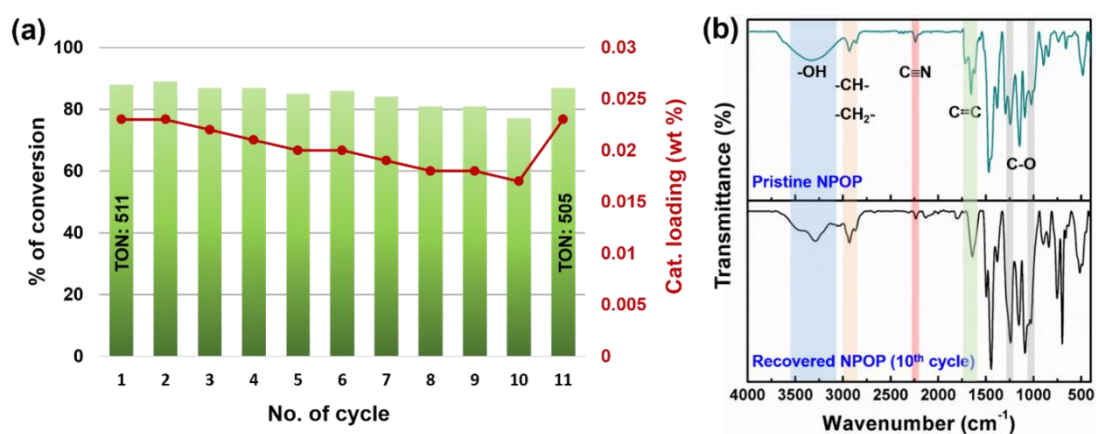

Fig. S11 (a) Recyclability of NPOP for catalytic conversion of styrene oxide and CO_2 to styrene carbonate. The amount of catalyst (wt%) in subsequent cycles is represented by red dots; the decrease in % of conversion is due to the weight loss of the catalyst (~ 1 mg/cycle) during the recovery process. The catalytic activity remains the same if the catalyst amount is maintained (30 mg), circumventing the weight loss, as shown in the 11th cycle. (b) FTIR spectra of pristine and recovered NPOP catalyst employed for CO_2 conversion reaction after 10 cycles.
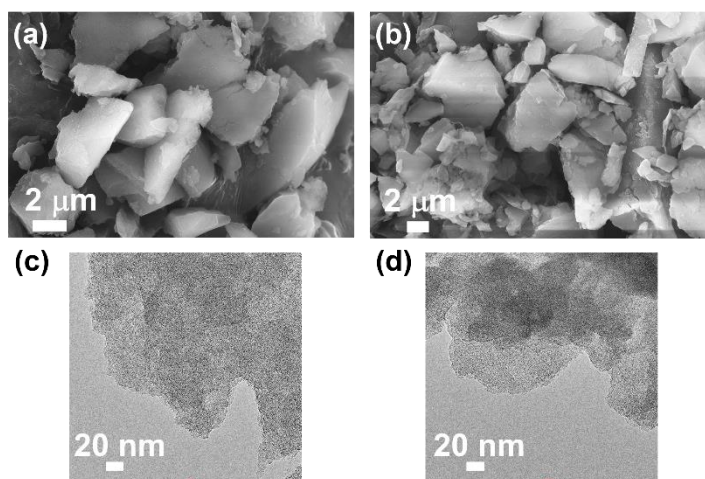

Fig. S12 (a, b) FESEM and (c, d) HRTEM images of pristine (a, c) and recovered NPOP (b, d), respectively employed for CO_2 conversion reaction after the 10th cycle.

structural integrity of the catalyst was reconfirmed by FTIR, FESEM, and HRTEM analysis (Fig. S11b, S12).

6. Fabrication and characterization of Ag@NPOP

6.1 Fabrication of silver nanoparticles encapsulated noria-based polymer (Ag@NPOP)

Well sonicated dispersion of 100 mg NPOP in 5 mL DMSO and 50 mg of $AgNO_3$ in DMSO (5 mL) were added to a 15 mL Schlenk-sealed tube (Scheme S3). The reaction mixture was stirred at room temperature for 2 h and then stirred at 80 °C for 24 h under a nitrogen atmosphere. The reaction mixture was allowed to cool to room temperature. The precipitate was separated by centrifugation and washed thoroughly with methanol and diethyl ether. The resulting dark-grey-colored solid was dried under vacuum at 80°C to yield Ag@NPOP. The formation of Ag(0) nanoparticles from Ag^+ was mediated by the oxidation of phenolic units present in NPOP.[15,16] The reducing property of NPOP was attributed to the polyphenolic noria core analogous to the reducing activity of natural polyphenols (e.g., flavonoids, tannic acid, etc.).
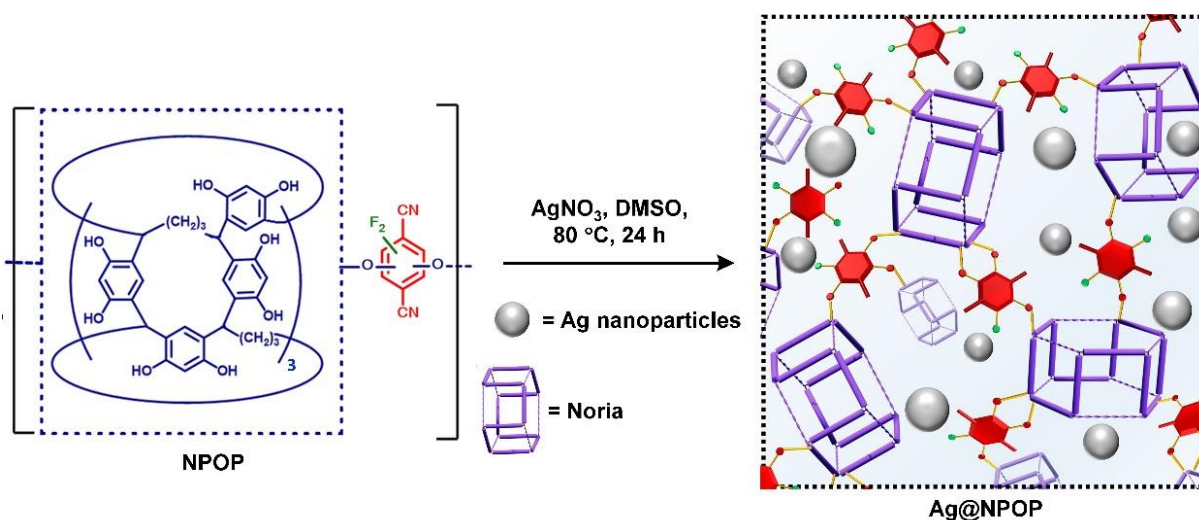
Scheme S3 Scheme for post-synthetically modified silver nanoparticles encapsulated noria-based polymer (Ag@NPOP); the size of Ag nanoparticles is not to scale as per the pore sizes of the networks in the pictorial depiction.

6.2 Microscopy and PXRD analysis

The HRTEM and high-angle annular dark-field scanning transmission electron microscopy (HAADF-STEM) images of Ag@NPOP showed a homogeneous distribution of spherical Ag nanoparticles throughout the polymer (Fig. S13a-e). A statistical estimate from the TEM images unveiled the average size of the Ag nanoparticles to be 6-15 nm. The crystalline nature of Ag@NPOP was ascertained through the selected area electron diffraction (SAED) pattern (Fig. S13d). PXRD pattern of Ag@NPOP showed the characteristics peaks of Ag (0) confirming the successful incorporation of Ag nanoparticles (JCPDS no. 04-0783) into the NPOP matrix (Fig. S13f).
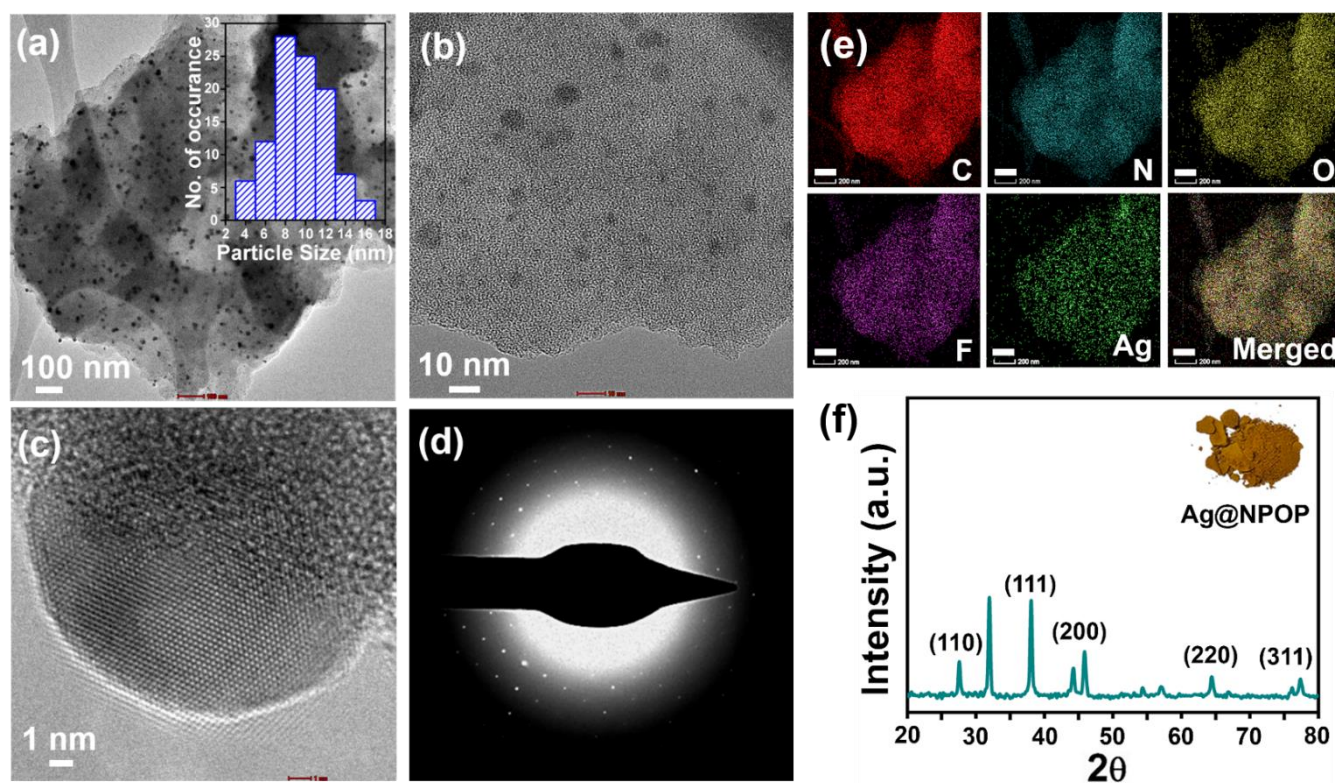

Fig. S13 (a) HRTEM image of Ag@NPOP, inset: statistical size distribution histogram of Ag nanoparticles on NPOP framework. (b) Magnified image of Ag@NPOP indicating the Ag nanoparticles embedded porous structure. (c) Lattice fringes due to the Ag nanoparticles in Ag@NPOP. (d) Selected area electron diffraction (SAED) pattern of Ag@NPOP. (e) High-angle annular dark-field scanning transmission electron microscopy (HAADF-STEM) elemental mapping images of Ag@NPOP indicating the homogeneous distribution of carbon, nitrogen, oxygen, fluorine, and silver throughout the network (scale = 200 nm). (f) PXRD profile of Ag@NPOP showing the representative diffraction peaks of Ag nanoparticles (JCPDS no. 04-0783).

6.3 Nitrogen gas sorption studies and porosity

The BET specific surface area of Ag@NPOP was found to be 100 m^2 g^{-1} (Fig. S14). The decrease in BET surface area compared to NPOP (773 m^2 g^{-1}) was due to the incorporation of Ag nanoparticles, which resulted in the blockage of the cavities.
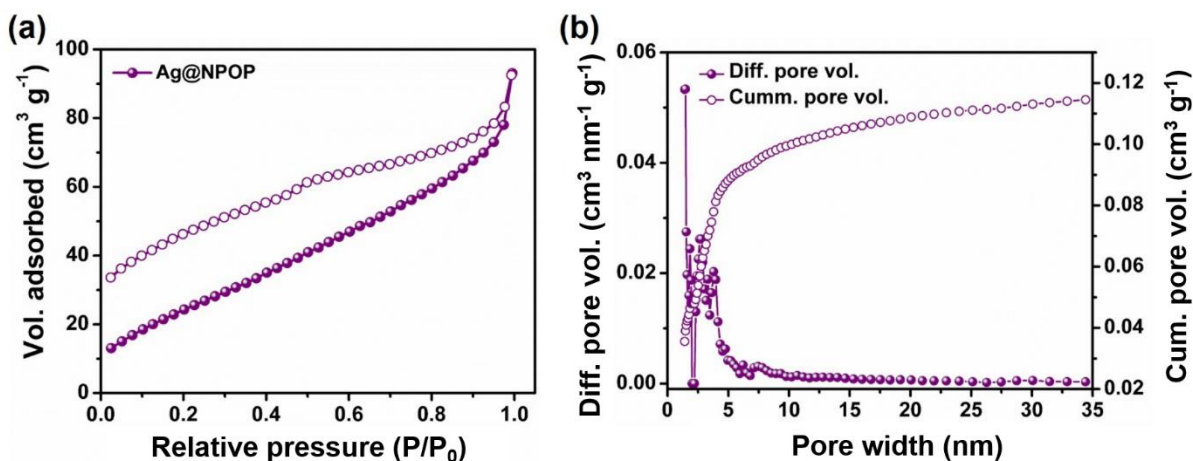

Fig. S14 (a) Nitrogen sorption isotherms (solid sphere: adsorption; hollow sphere: desorption) of Ag@NPOP. (b) NLDFT pore size distribution of Ag@NPOP (solid sphere: differential pore volume vs. pore width plot; hollow sphere: cumulative pore volume vs. pore width plot).

6.4 XPS analysis

The XPS analysis of POPs is shown in Fig. S15. The fitting parameter (χ^2) values in all cases were close to 1. The C 1s spectrum of Ag@NPOP revealed the presence of sp^3-C at 284.4 eV, whereas the C-O peak appeared at 286.2 eV. O 1s spectrum indicated the presence of –OH, C=O, and C-O-C at 530.1, 531.1, and 532.8 eV, respectively. The C=O bonds might appear due to the oxidation of the phenolic –OH group upon silver loading.[15,16] On the other hand, peaks at 687.1 and 685.3 eV in F 1s spectra were assigned to two different types of binding modes of tetrafluoroterephthalonitrile moiety with noria core.[10] Peaks at 368.3 and 374.3 eV (with a spin energy separation of 6 eV) were attributed to Ag(0) 3d$_{5/2}$ and Ag(0) 3d$_{3/2}$, respectively, ascertaining the formation of silver nanoparticles.
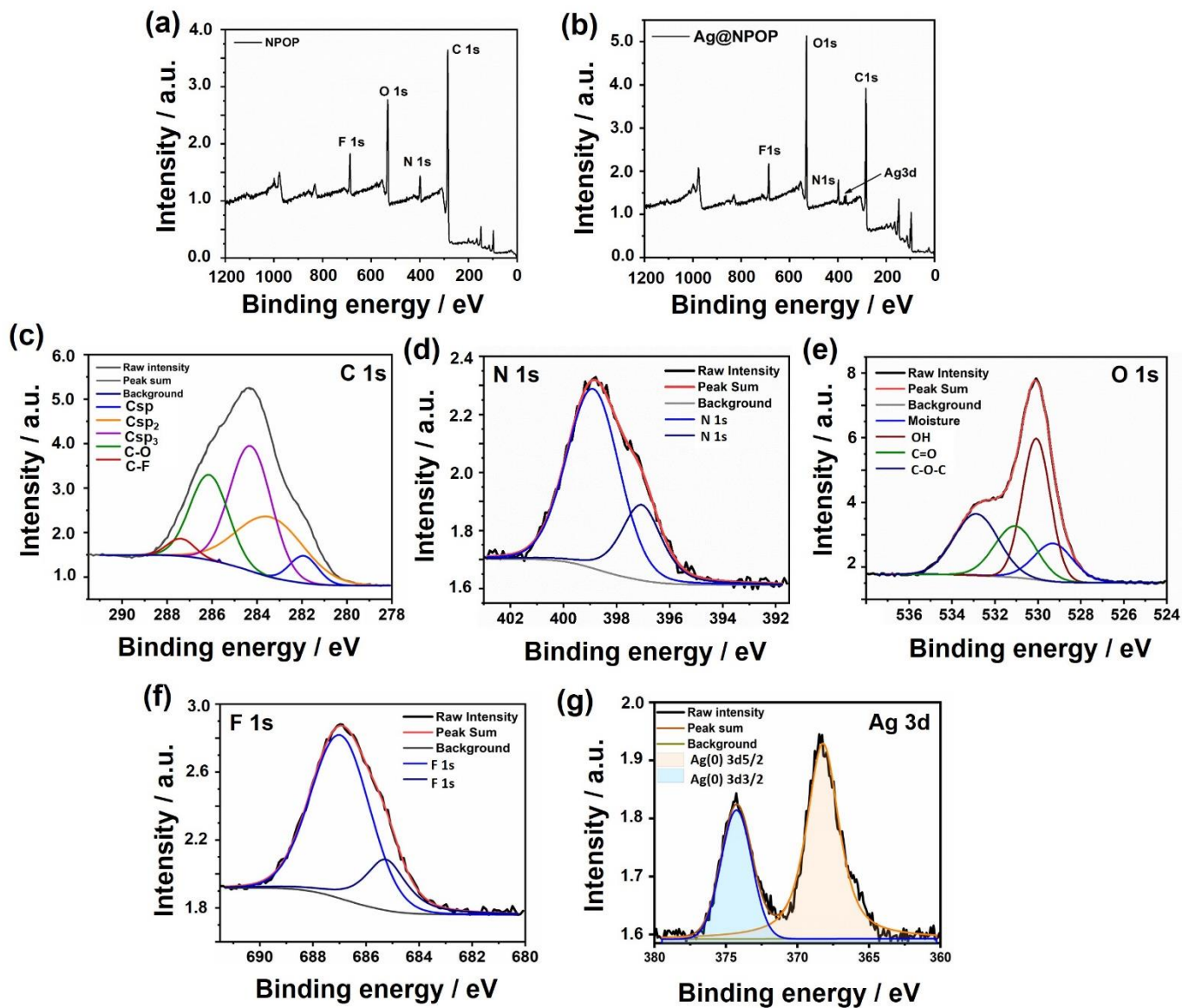
Fig. S15 X-ray photoelectron spectroscopy analysis: (a) full spectrum of NPOP, and (b) full spectrum of Ag@NPOP, (c) C 1s, (d) N 1s, (e) O 1s, (f) F 1s, and (g) Ag 3d of Ag@NPOP.

7. Ag@NPOP as heterogeneous catalyst

7.1 Catalytic reduction of 4-nitrophenol

The catalytic reduction of 4-nitrophenol in the presence of sodium borohydride ($NaBH_4$) has emerged as a key method based on the simplicity and low cost. 4-aminophenol is non-toxic and commonly used for analgesics and antipyretics in the pharmaceutical industry, such as for the synthesis of paracetamol, phenacetin, etc.[17] Hence, Ag@NPOP was employed for the catalytic reduction of 4-nitrophenol to 4-aminophenol (Scheme S4).
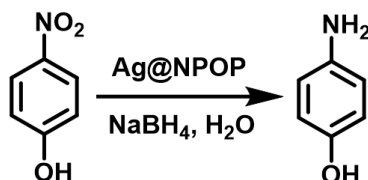
Scheme S4 Schematic illustration of the catalytic reduction of 4-nitrophenol using Ag@NPOP.

The aqueous solution of *p*-nitrophenol (0.13 mM) and aq. sodium borohydride (0.2 M) was taken into a cuvette. A water suspension of Ag@NPOP (1 mg mL^{-1}, 50-100 µL) was added, and the progress of the reaction was monitored by UV-Vis spectroscopy at room temperature. The reaction conditions were optimized by changing the concentration of nitrophenol, $NaBH_4$, and catalyst (Table S4, Fig. S16).

Table S4 Catalytic reduction of 4-nitrophenol using Ag@NPOP with varying concentrations of substrate and catalyst.

4-Nitrophenol	NaBH$_4$	Catalyst (1 mg/mL)	Time (99% conversion)
0.13 mM	0.2 M	-	No conversion (2 days)
0.13 mM	0.2 M	225 µL (commercial AgNP)	30 min
0.13 mM	0.2 M	50 µL (Ag@NPOP)	4.5 min
0.13 mM	0.1 M	50 µL (Ag@NPOP)	5.5 min
0.13 mM	0.05 M	50 µL (Ag@NPOP)	14 min
0.13 mM	0.05 M	100 µL (Ag@NPOP)	12 min

In the beginning, the light-yellow color of nitrophenol changed to bright yellow after the addition of NaBH$_4$ solution due to the formation of 4-nitrophenolate. When the Ag@NPOP catalyst was added, the solution became colorless. The absorption peak at 408 nm, corresponding to a bright yellow solution, decreased. In contrast, the peak at ~300 nm simultaneously increased, corresponding to 4-nitroaniline. Reaction under similar conditions without Ag@NPOP showed no conversion. Progress of the reaction was observed by plotting the change in percentage of conversion with time. Facile diffusion of the reactant through the pores and easy accessibility of the catalyst over a porous surface significantly enhanced the reaction rate. Since the concentration of NaBH$_4$ was considerably higher than that of 4-nitrophenol, the order of the reaction was labeled as a pseudo-first-order reaction.[18] The rate-constant was estimated to be 1.60×10^{-2} sec^{-1}.
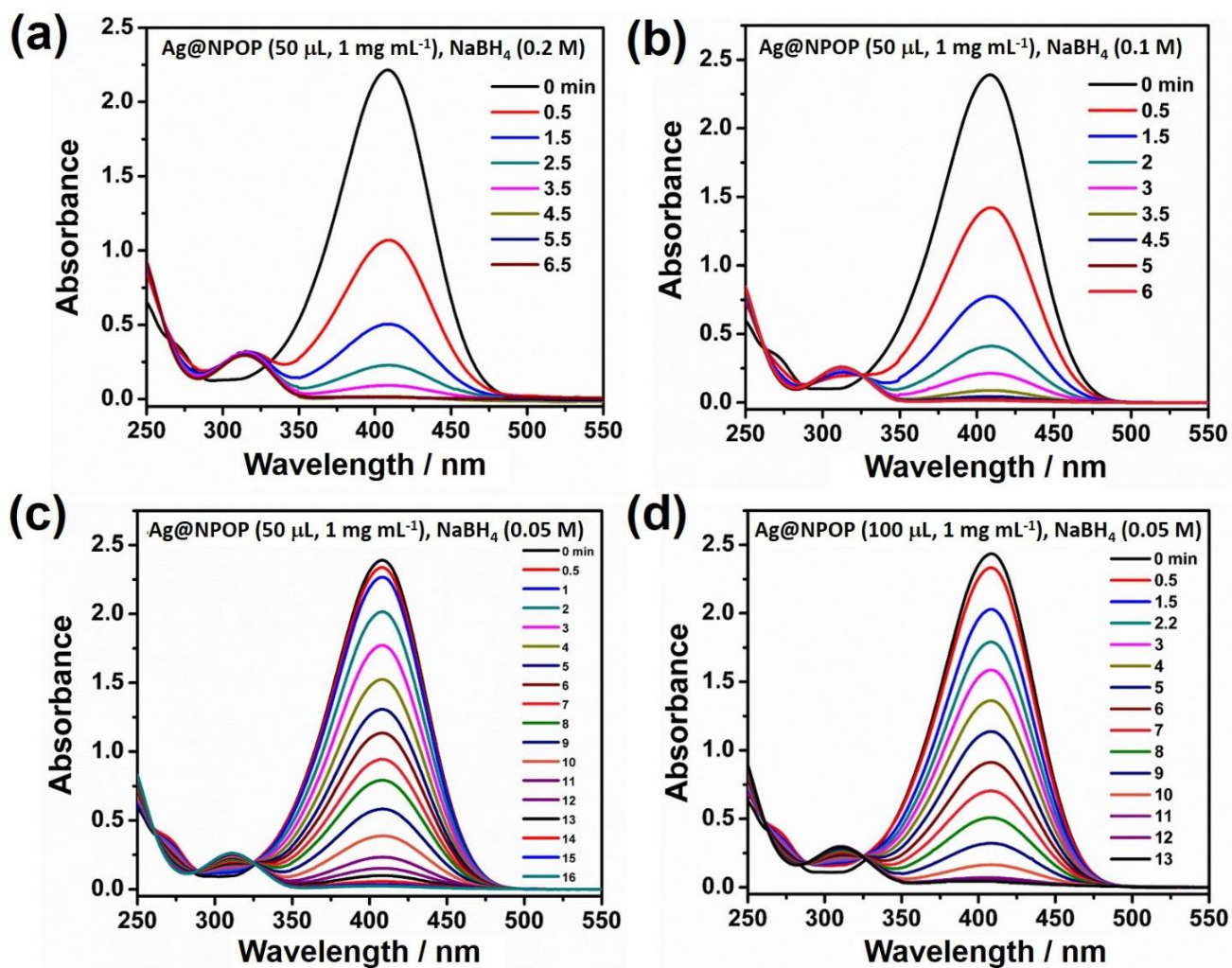

Fig. S16 Ultraviolet-visible spectra at successive time intervals for the conversion of 4-nitrophenol to 4-aminophenol by varying amount of Ag@NPOP and NaBH$_4$ (a-d).
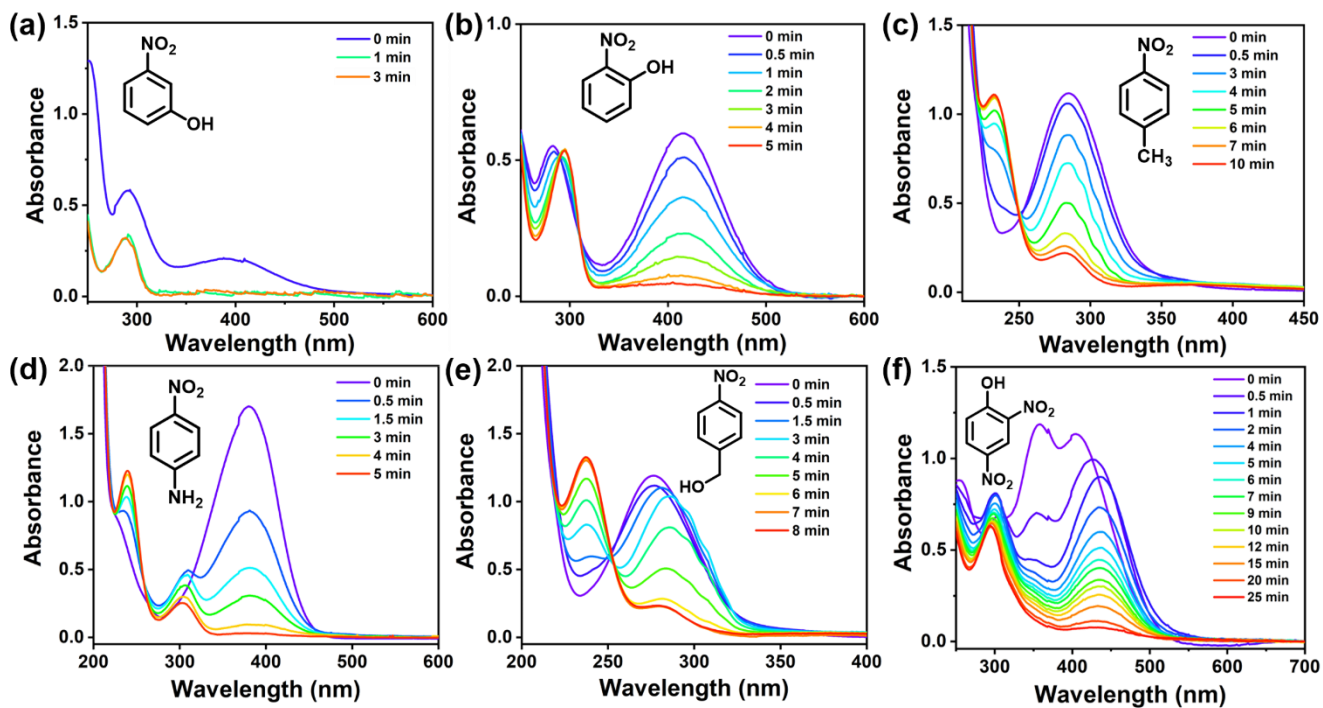
Fig. S17. Ultraviolet-visible spectra at successive time intervals depicting the conversion of (a) 3-nitrophenol, (b) 2-nitrophenol, (c) 4-nitrotoluene, (d) 4-nitroaniline, (e) 4-nitrobenzyl alcohol, (f) 2,4-dinitrophenol, respectively, catalyzed by Ag@NPOP. Substrate (0.13 mM), NaBH$_4$ (0.2 M), catalyst (1 mg mL^{-1}).

We performed UV-visible spectroscopic investigation for the reduction of different nitroarenes [(0.13 mM, in water or water:ethanol mixture (5:1 v/v)] by Ag@NPOP (1 mg mL^{-1}, 100 μL in 2.3 mL reaction mixture) in the presence of hydride donor NaBH$_4$ (0.2 M, Fig. S17). Ag@NPOP showed fast reduction of various nitroarenes, including 4-nitrophenol (~98% in 4 min), 3-nitrophenol (~95% in 3 min), 2-

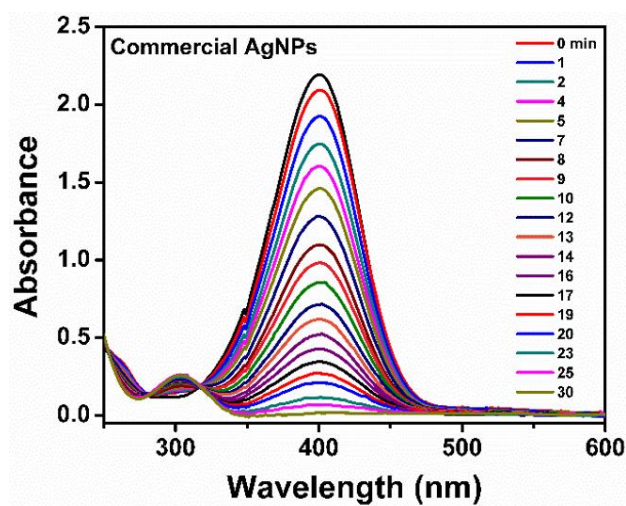

Fig. S18 Ultraviolet-visible spectra at successive time intervals for the conversion of 4-nitrophenol (0.13 mM) to 4-aminophenol by commercial Ag nanoparticles (225 μL of 0.02 mg mL^{-1}), and NaBH$_4$ (0.2 M).

nitrophenol (~93% in 5 min), 4-nitrotoluene (~80% in 10 min), 4-nitroaniline (~98% in 5 min), 4-nitrobenzyl alcohol (~80% in 10 min), and 2,4-dinitrophenol (~90% in 25 min). We further checked the catalytic efficiency using commercially available Ag nanoparticles (Sigma-Aldrich, Catalogue no. 730777) dispersion for the same reaction under similar conditions. 4-Nitrophenol (0.13 mM) reduction in the presence of 0.2 M $NaBH_4$ catalyzed by Ag nanoparticles (225 μL of 0.02 mg mL^{-1} equivalent to 9 wt% Ag, ~1.5 times higher Ag wt% than in Ag@NPOP) would take 30 mins compared to 4.5 min by Ag@NPOP, suggesting the superiority of the later as catalyst (Fig. S18).

For the bulk scale reaction, nitroarenes (1 mmol) and NaBH4 (8 mmol) were dissolved in ethanol (15 mL), and 30 mg of Ag@NPOP was dispersed into it. The mixture was stirred at room temperature for 2 h under a nitrogen atmosphere. The catalyst was separated after the reaction by centrifugation. After the workup, the crude reaction mixture was checked for NMR to determine the % of conversion (Fig. S38-S40).

The reduction of nitroarenes is likely to proceed through four consecutive steps, (i) adsorption of nitroarenes on the porous network of Ag@NPOP; (ii) adsorption of molecular hydrogen released from NaBH4 on the catalytically active centers, i.e., silver nanoparticles, encapsulated into the heteroatom-rich porous framework, (iii) transfer of hydrogen to nitroarenes mediated by metal nanoparticles. Finally, (iv) desorption of aromatic amines from the catalyst surface. It has been proposed in the literature that the conversion of 4-aminophenol from 4-nitrophenol in the presence of silver nanoparticles involves the formation of 4-nitrosophenol and 4-(hydroxyamino)phenol as intermediates (Fig. S19).[18-20]
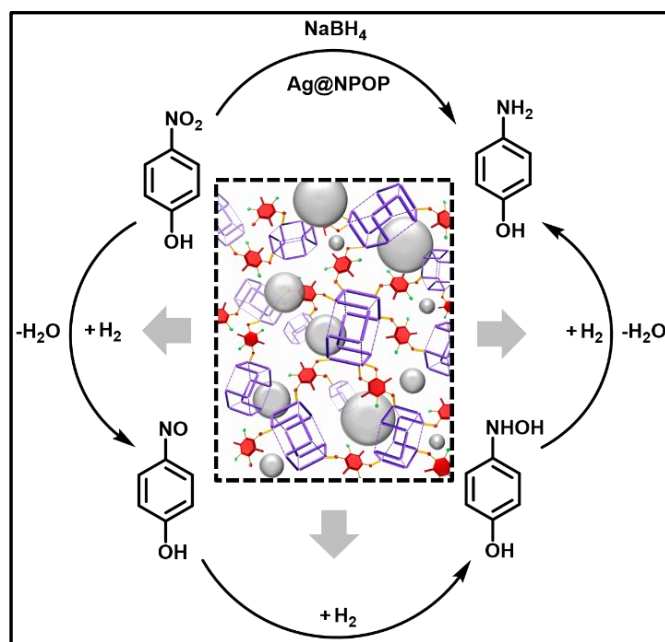

Fig. S19 Schematic illustration of the catalytic reduction of 4-nitrophenol to 4-aminophenol by Ag@NPOP. Particle sizes of silver nanoparticles are not to scale as per the pore sizes of the frameworks in the pictorial depiction.

7.2 Recyclability

The Ag@NPOP was recovered by centrifugation, and reactivated by washing with water, methanol, and dried under vacuum at 70°C for 6 h after every use. The catalyst was highly effective in reducing 4-nitrophenol, giving ~ 95% conversion for consecutive 15 cycles (Fig. S20a). The FTIR spectrum of the recovered catalyst was found to be the same as that of the pristine one (Fig. S20b). The thermogravimetric analysis of Ag@NPOP after the hot water filtration study indicated no loss of silver. The ICP-OES analysis of recovered Ag@NPOP suggested negligible loss (~ 0.6 wt%) of Ag, signifying the robustness of the catalyst. FESEM and HAADF-STEM images suggested the unaltered morphology with homogeneous distribution of Ag nanoparticles throughout the NPOP matrix (Fig. S21 and S22).
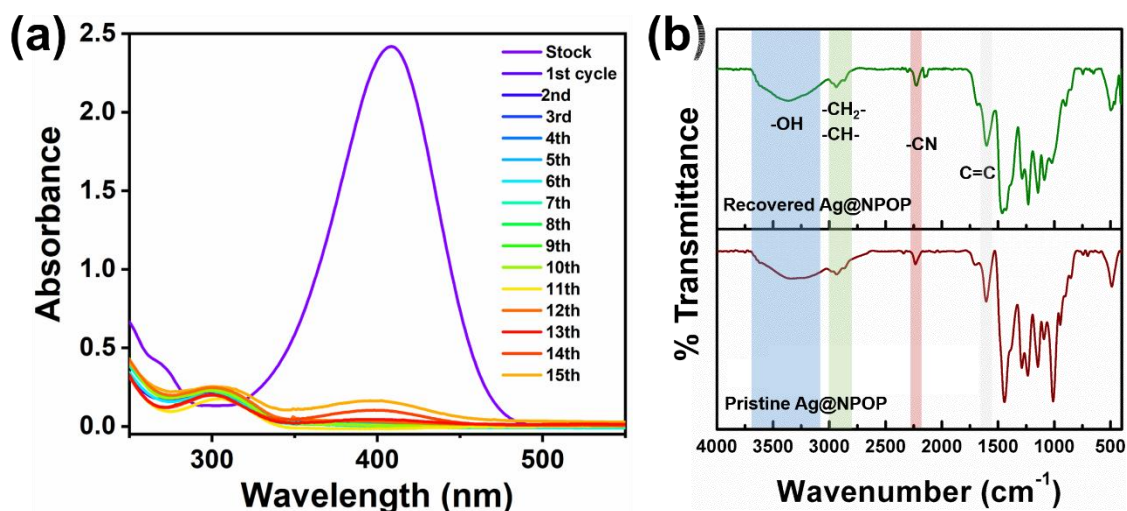

Fig. S20 (a) UV-vis absorption spectra monitoring the 4-nitrophenol reduction by Ag@NPOP for consecutive 15 cycles. (b) FTIR spectra of pristine (brown) and recovered (green) Ag@NPOP catalyst employed for 4-nitrophenol reduction after the 15th cycle.
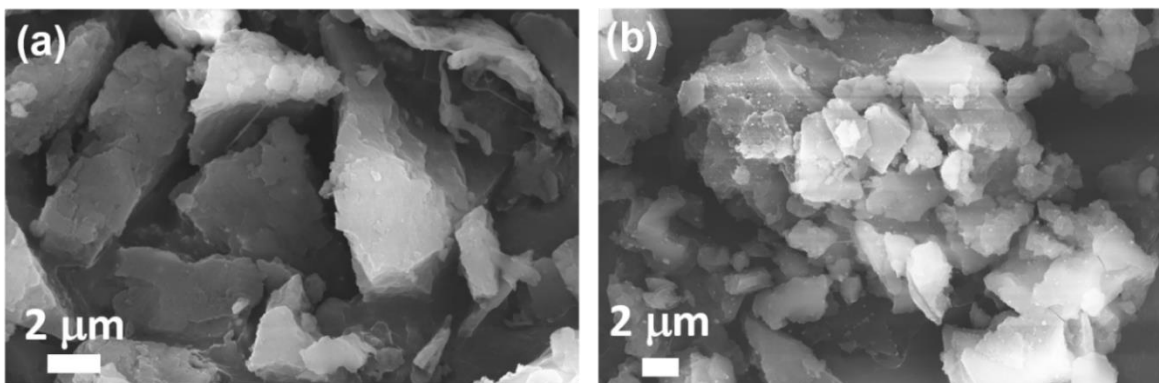

Fig. S21 FESEM images of (a) pristine and (b) recovered Ag@NPOP employed for 4-nitrophenol reduction after 15 consecutive cycles.
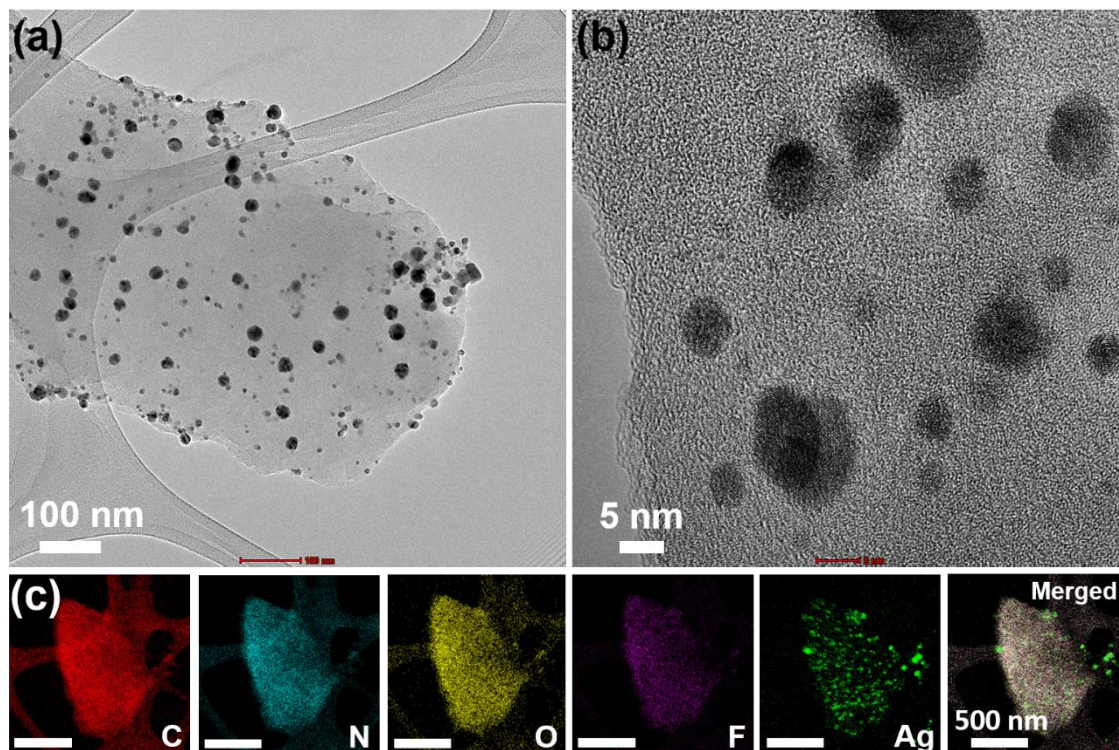
Fig. S22 (a, b) HRTEM images of recovered Ag@NPOP employed for 4-nitrophenol reduction after the 15th cycle. (c) HAADF-STEM images indicate that the homogeneous distribution of silver nanoparticles is retained after catalysis; scale = 500 nm.

7.3 Three-component coupling reactions

We performed a one-pot three-component coupling reaction among the aromatic aldehyde, cyclic secondary amine, and terminal alkyne for the synthesis of propargylamine derivative catalyzed by Ag@NPOP. First, the catalyst (15 mg), aldehyde (1 mmol), cyclic secondary amine (1.1 mmol), phenylacetylene (1.5 mmol), and THF (1 mL) were taken in a 5 mL round bottom flask. The reaction
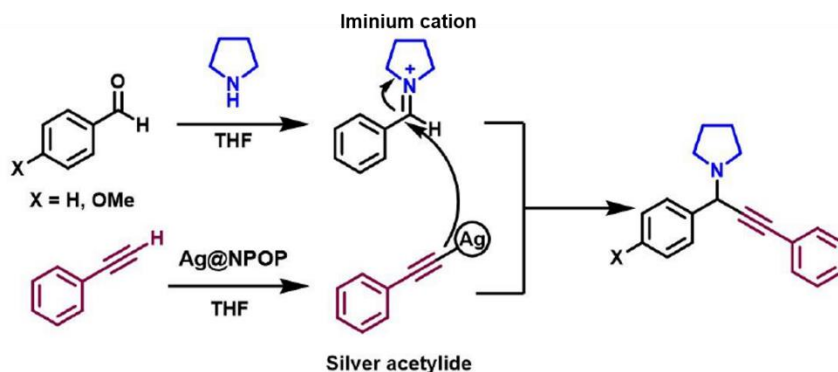

Fig. S23 Plausible mechanism of three-component coupling reaction of aldehyde, cyclic secondary amine, and terminal alkyne for the formation of propargylamine [1-(1,3-diphenylprop-2-yn-1-yl)pyrrolidine] catalyzed by Ag@NPOP.

mixture was stirred for 12 h under a nitrogen atmosphere at 70°C. Then the catalyst was separated by filtration, and the solvent was evaporated under reduced pressure. The % of conversion was calculated by ^{1}H NMR analysis with respect to the corresponding aldehyde. We obtained ~64% and ~70 % of conversion for 4-methoxybenzaldehyde and benzaldehyde, respectively, by Ag@NPOP (Fig. S41-S44), which could be improved through further optimizations. The plausible mechanism was proposed in Fig. S23. First, the activation of the C-H bond of alkyne was induced by silver nanoparticles encapsulated in Ag@NPOP. The resultant silver acetylide species reacted with the *in situ* generated iminium ion from aromatic aldehyde and cyclic secondary amine that led to the formation of propargylamine.[21-24] The catalyst can be recycled multiple times without significant loss in the catalytic efficiency (Fig. S24). The synthesis of propargylamine derivative [1-(1,3-diphenylprop-2-yn-1-yl)pyrrolidine] through a heterogeneous catalytic route using metal loaded porous organic polymers, to the best of our knowledge, has not been demonstrated yet. However, further detailed study encompassing solvent screening and variable reaction conditions is required to improve the efficiency of the Ag@NPOP catalyst.
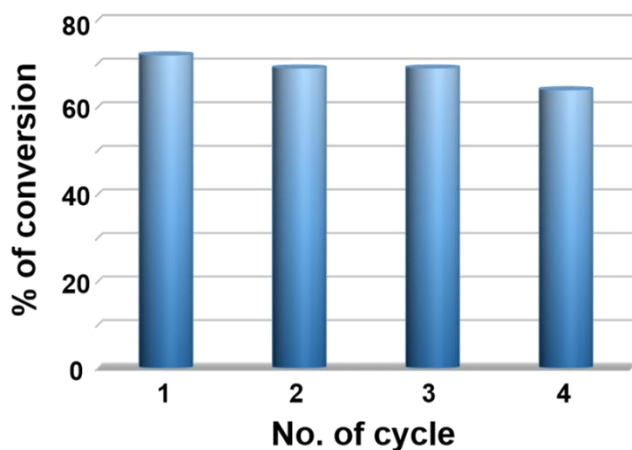

Fig. S24 Recyclability of Ag@NPOP shown up to the 4th cycle for the synthesis of propargylamine derivative [1-(1,3-diphenylprop-2-yn-1-yl)pyrrolidine] in a three-component reaction.

8. Comparative accounts of cavitand/cage based porous organic polymers

Table S5 Comparative accounts of noria-based porous organic polymers (POPs) developed in the present study with other cavitand/ cage-based porous organic polymers for heterogeneous catalysis.

S. No.	Substance	Cavitand/ cage used	Surface area (S_{BET}: m^2 g^{-1})	Catalysis	Reference
1.	NPOP*	Noria cage	773	Metal-free CO_2 conversion to cyclic organic carbonates	*Present work**
	Ag@NPOP		100	Nitrophenol reduction, one pot three component reaction (aldehyde, amine and alkyne) for the synthesis of propargylamine derivatives	
Cavitand-based porous organic polymers					
2.	CDPs-HIPE-TiO$_2$	Cyclodextrin	171	Photocatalytic degradation of Methylene blue	*Small,* 2020, **16**, 1907555.[25]
3.	CD-PAF		-	Halogenation of aryl compounds	*ACS Appl. Mater. Interfaces,* 2017, **9**, 30958.[26]
4.	BnCD-HCPP		1225	Nitrophenol reduction	*Chem. Sci.,* 2016, **7**, 905.[27]
5.	RN4-Az-OH	Resorcin[4]arene	340	Metal-free CO_2 conversion to cyclic organic carbonates	*Chem. Mater.,* 2019, **31**, 8440.[4]
6.	CalCOP-1	Calix[4]arene	46	Metal-free CO_2 conversion to cyclic organic carbonates	*Ind. Eng. Chem. Res.* 2020, **59**, 7247.[28]
7.	Pd-PPQ	Pillar[5]arene	202	Suzuki coupling reactions	*ChemCatChem,* 2019, **11**, 2864.[29]
8.	TADP5Ti		-	Asymmetric reduction of aldehyde	*Polym. Chem.,* 2017, **8**, 7108.[30]

*To the best of our knowledge, there is no report on organic molecular cage-based porous organic polymers for heterogeneous catalysis.

Table S6 A comparative account of CO_2 conversion to cyclic organic carbonates by NPOP in comparison with the other reported catalysts, including homogeneous catalysts, inorganic complexes, metal organic frameworks, covalent organic frameworks, ionic liquids, cage compounds, porous silica-based materials, metal loaded polymers (M@POPs), and porous organic polymers.

S. No	Substance	Pressure (bar)	Temp. (ºC)	TBAB	Conversion of propylene oxide (%), time (h)	Reference
1.	Noria				84 (12) [styrene oxide]	Present work (metal-free, solvent-free CO_2 fixation)
2.	NPOP	2.5	90	0.3 mmol	88 (12) [styrene oxide] 99 (12) [propylene oxide] 98% (12) [epichlorohydrin][#]	
Homogeneous catalysts						
3.	Al-catalyst C*	10	25	5	99 (14)	Angew. Chem. Int. Ed., 2016, **55**, 3972.[31]
4.	Squaramide-5*	10	45	5 mol% (TBAI)	74 (18)	ACS Catal. 2017, **7**, 3532.[32]
5.	V (V) Complex-3*	10	85	0.25 (TBAI)	74 (18)	ACS Catal. 2017, **7**, 2367.[33]
Metal loaded covalent organic frameworks (M@COFs)						
6.	2,3-DhaTph	1	110	0.05	94 (12 h)	Catal. Sci. Technol., 2016, **6**, 6152.[34]
7.	COF-JLU6	1	40	0.51	88 (48)	J. Mater. Chem. A, 2018, **6**, 374.[35]
8.	TBICOF	1	28	0.5	54 (24)	Chem. Mater., 2019, **31**, 1584.[36]
9.	COF-HNU14 (Imidazolium salt)	20	120	-	96 (24)	ACS Sustainable Chem. Eng., 2020, **8**, 18413.[37]
10.	Zn-Salen-COF-SDU113	1	25	1.8	98 (48)	Nat. Commun., 2020, **11**, 4481.[38]
Metal organic frameworks (MOFs)						
11.	ZIF-8/CN	10	80	-	99 (24)[#]	Adv. Funct. Mater., 2017, **27**, 1700706.[39]
12.	Acrylamide-containing MOF	1	RT	0.5 g	96 (48)	Chem. Mater., 2017, **29**, 9256.[40]
13.	Zn-DPA	10	100	0.3	99 (2)	Nat. Commun., 2019, **10**, 4362.[41]
14.	Zn(II) organic framework with a $Zn_4(-COO)_6$ cluster	1 atm	30-40	1 mol%	99 (24)	Chem. Eur. J. 2020, **26**, 788.[42]
Ionic liquids						
15.	PDMBr (ionic liquid)	10	110	-	99 (4)	Chem. Sci., 2015, **6**, 6916.[43]
16.	KCC-1/IL/HPW NPs	10	90	-	98 (1.5)	Green Chem., 2015, **17**, 3059.[44]

					Metal encapsulated cage compounds	
17.	Co(III)@cage	1	25	10 mol%	58 (48) / 99 (24 h)[#]	*Chem. Sci.*, 2019, **10**, 1549.[45]
18.	Cg-Am*	2.5	90	2.5 mol%	95 (9)	*Sustainable Energy Fuels*, 2019, **3**, 2567.[46]
					Metal loaded porous organic polymers (M@POPs)	
19.	Co-CMP	30	100	1.8 mol%	98 (1)	*Nat. Commun.*, 2013, **4**, 1960.[47]
20.	Zn(OAc)$_2$ loaded o-Hydroxyazo POPs	30	100	7.2 mol%	90 (0.8)	*Angew. Chem. Int. Ed.*, 2016, **55**, 9685.[48]
21.	Co/Zn R@HMTA	10	100	7.2 mol%	99 (1.5)	*Adv. Mater.*, 2017, **29**, 1700445.[49]
22.	Zn/RN4-Az-OH	1	35	0.25	92 (24)[#]	*Chem. Mater.*, 2019, **31**, 8440.[4]
23.	Zn/POF2	2.5	90	0.43	90 (9)	*Chem. Sci.*, 2020, **11**, 7910.[50]
					Porous organic polymers (POPs)	
24.	N-Heterocyclic carbenes polymers	1	120	10 mol%	98 (24)	*Chem. Mater.*, 2015, **27**, 6818.[51]
25.	Porphyrin-based POPs	15	100	1 mol%	99 (5)	*Green Chem.*, 2018, **20**, 903.[52]
26.	COP-222	1	100	-	99 (24)	*Chem*, 2019, **5**, 3232.[53]
27.	N-rich click-based POP (CPP)	1	100	-	99 (24)	*ChemSusChem*, 2020, **13**, 180.[54]

*Nonrecyclable, [#]Epichlorohydrin used as the substrate, catalysis further assisted by the anchimeric assistance of –Cl group

Table S7 Comparative accounts of silver nanoparticles loaded noria-based porous organic polymer (Ag@NPOP) with some of the well-known metal loaded porous materials, like porous organic polymers (POPs), covalent organic frameworks (COFs), metal organic frameworks (MOFs), porous silica, and cage molecules for catalytic reduction of nitrophenol.

S. No.	Catalyst	Substrate and NaBH$_4$	Pseudo-first order rate constant (s^{-1})	Time	References
1	Ag@NPOP	0.13 mM, 0.2 M (NaBH$_4$)	1.6×10^{-2} s^{-1}	4.5 min	*Present work*
			Metal loaded Covalent Organic Frameworks (M@COFs)		
2	Au(0)@TpPa-1	15 mL, 0.18 mmol/L 162.3 mg in 12 ml (NaBH$_4$)	5.3×10^{-3} s^{-1}	13 min	*Chem. Commun.*, 2014, **50**, 3169.[55]
3	Au/COF	0.18 mM 15 mL, 0.36 M 12 mL NaBH4	7.6×10^{-3} s^{-1}	10 min	*ACS Appl. Mater. Interfaces* 2017, **9**, 7481.[56]
4	PtNPs@COF	1.0×10^{-3} M, 0.3 mL 0.5 M, 1 mL (NaBH$_4$)	-	8 min	*J. Am. Chem. Soc.*, 2017, **139**, 17082.[57]

5	UiO-66 NH$_2$@COP@Pd	30 μL, 0.01 M, 0.25 mL of NaBH$_4$ (0.19 M)	5.2×10^{-3} s^{-1}	6 -7 min	*ACS Appl. Mater. Interfaces* 2020, **12**, 7285.[58]
6	PtNPs@Phos-COF-1	1.5×10^{-2} M, 2.0 mL 20 M, 2.0 mL (NaBH$_4$)	-	7 min	*Small*, 2020, **16**, 1906005.[59]
Metal loaded Porous Organic Polymers (M@POPs)					
7	Au@BnCDHCPP	0.1 mM 0.3 M, 0.1 mL (NaBH$_4$)	-	3 min	*Chem. Sci.*, 2016, **7**, 905.[27]
8	Au@Im-POP-2	0.5 mmol 2.5 mmol (NaBH$_4$)	-	60 min	*Dalton Trans.*, 2016, **45**, 16896.[60]
9	Ag0@CMP	10 mL, 10 mmol L^{-1} 1.0 mL, 1.0 mol L^{-1} (NaBH$_4$)	8.1×10^{-2} s^{-1}	60 min	*ACS Appl. Mater. Interfaces*, 2017, **9**, 5231.[61]
10	Ag0@CZ–TEB	1 mL, 0.05 mol L^{-1} 1.0 mL, 5.0 mol L^{-1} (NaBH$_4$)	1.9×10^{-2} s^{-1}	2 min	*J. Mater. Chem. A*, 2019, **7**, 13449.[62]
Metal Organic Frameworks					
11	Pt/NPC-900 Ni/NPC-900	20 mg L^{-1} 3 mg (KBH$_4$)	-	3-6 min	*ACS Appl. Mater. Interfaces* 2018, **10**, 12740.[63]
12	NU-1000-Au-nano	5 mg 20 mg (NaBH$_4$)	4×10^{-3} s^{-1}	14 min	*Chem. Mater.*, 2019, **31**, 1485.[64]
13	ZIF-8@Au25@ZIF-67	3.33 mmol L^{-1}, 60 μL 0.42 molL^{-1}, 70 μL (NaBH$_4$)	-	3 min	*J. Am. Chem. Soc.*, 2020, **142**, 9, 4126.[65]
Organic Cages					
14	Pd@MTC1-1/5	5.0 μL, 0.06 mol L^{-1} 0.13 mmol	-	5 min	*Angew. Chem. Int. Ed.*, 2019, **58**,18011.[66]
15	Pd@RCC3	0.165 mmol L^{-1}, 0.264 mmol NaBH$_4$	2×10^{-2} s^{-1}	4 min	*Nat. Catal.*, 2018, **1**, 214.[67]
16	Au@o-DPC Au@c-DPC	30 μL, (10 mM) 10 mM, 300 μL (NaBH$_4$)	4.1×10^{-2} s^{-1} 1.7×10^{-2} s^{-1}	2-4 min	*Dalton Trans.*, 2020, **49**, 12145.[68]
Porous silica composite					
17	Ag-DHSS	1.8 mg/mL, 10 mL -	-	40 min	*Chem. Mater.*, 2016, **28**, 5596.[69]
18	Heterobimetallic Co−Mn oxide (Co$_2$Mn$_3$O$_8$)	200 μM 3 mL, 0.05 M 300 μL of NaBH$_4$	1×10^{-3} s^{-1}	10 min	*ACS Sustainable Chem. Eng.* 2017, **5**, 11504.[70]
19	SBA-15/PDA0.6/Ag	0.2 mL, 20 mM 0.660 mL, 3 M (NaBH$_4$)	1.5×10^{-2} s^{-1}	7 min	*ACS Appl. Mater. Interfaces*, 2018, **10**, 1792.[71]
20	Mo-doped Ni-based catalyst (MNC)	NP (0.125 mM) and NaBH$_4$ (1.0 M)	9.2×10^{-3} s^{-1}	7 min	*ACS Appl. Nano Mater.*, 2019, **2**, 879.[72]

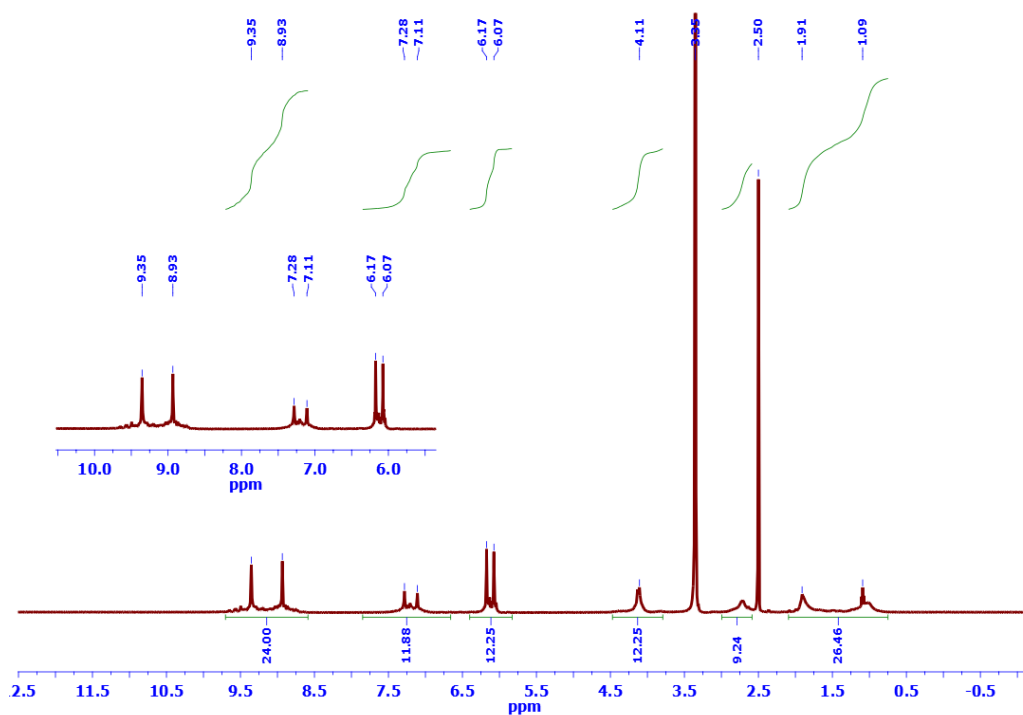# 9. ¹H, ¹³C NMR and mass analysis

Fig. S25 ¹H NMR spectrum (500 MHz) of noria in D₆-DMSO.
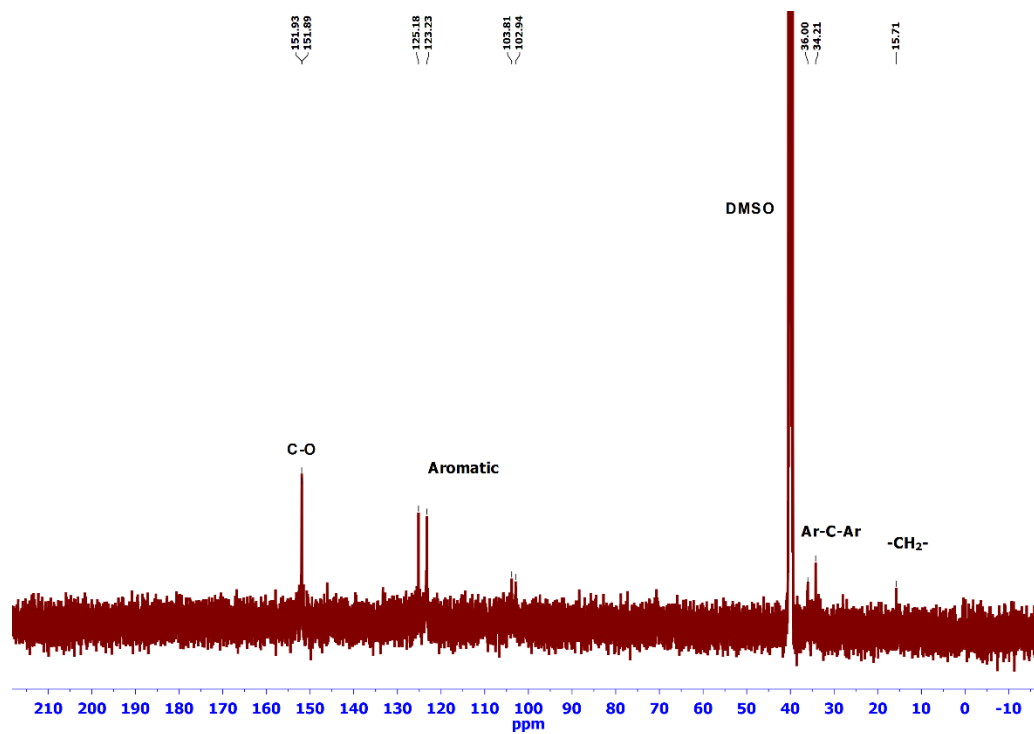

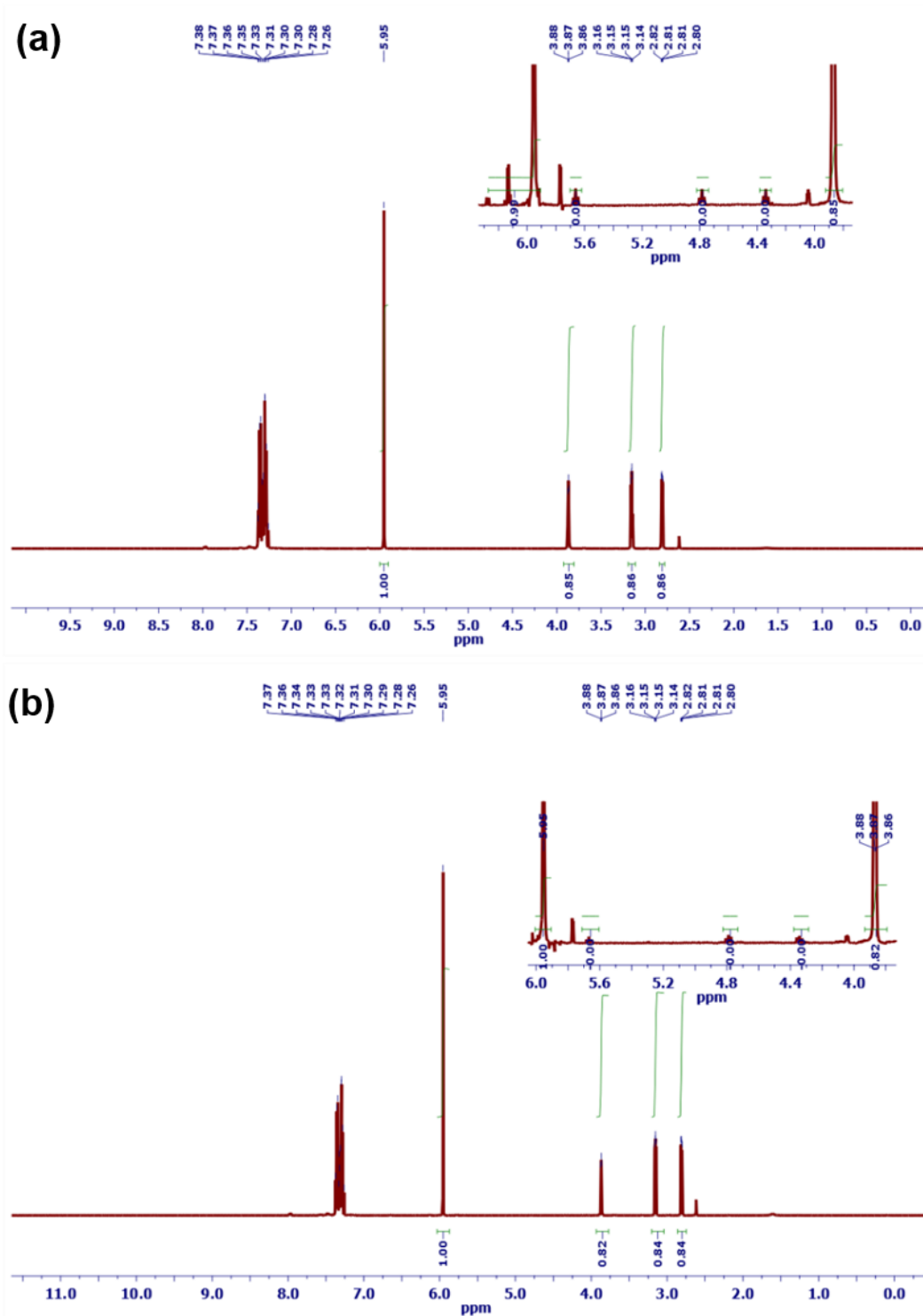**Fig. S26** ¹³C NMR spectrum (126 MHz) of noria in D₆-DMSO.

Fig. S27 ^{1}H NMR spectra of the reaction mixture in CDCl$_3$ for the reaction of styrene oxide and CO$_2$ employing (a) noria and (b) NPOP as the catalyst and in the absence of cocatalyst, tetrabutylammonium bromide (TBAB), indicating only a trace amount of conversion into corresponding cyclic organic carbonate.
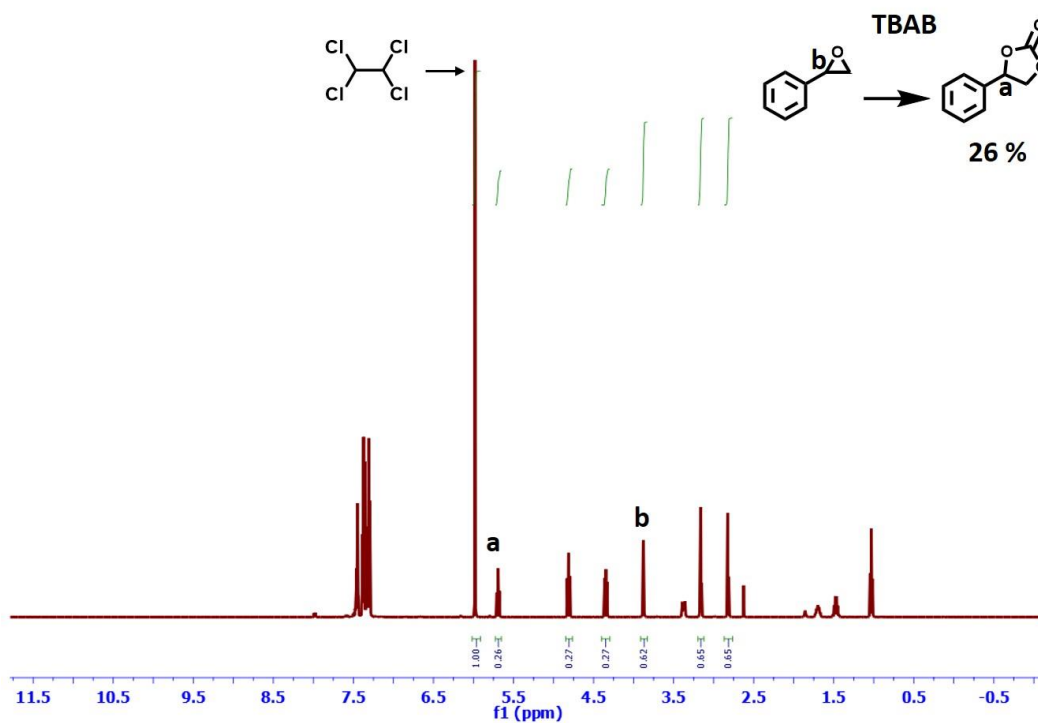
Fig. S28 ^{1}H NMR spectrum of the reaction mixture (in CDCl$_3$) for the conversion of styrene oxide with tetrabutyl ammonium bromide (TBAB) as the only catalyst using 1,1,2,2-tetrachloroethane as external NMR standard.
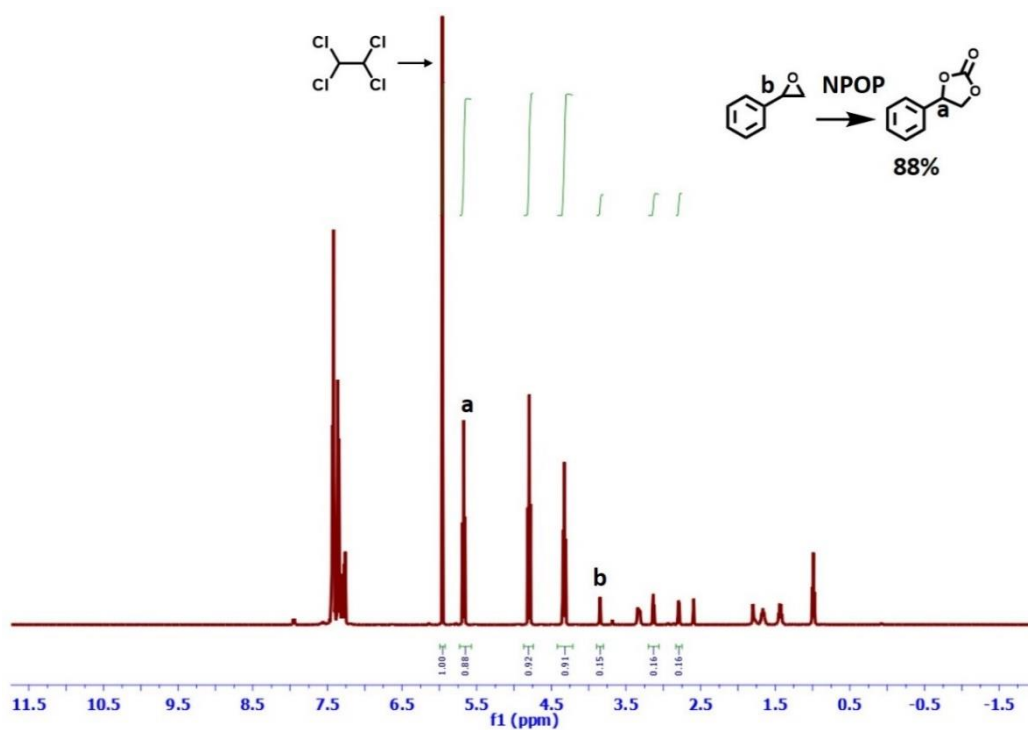
Fig. S29 ^{1}H NMR spectrum of the reaction mixture (in CDCl$_3$) for the conversion of styrene oxide with NPOP as a catalyst using 1,1,2,2-tetrachloroethane as external NMR standard.
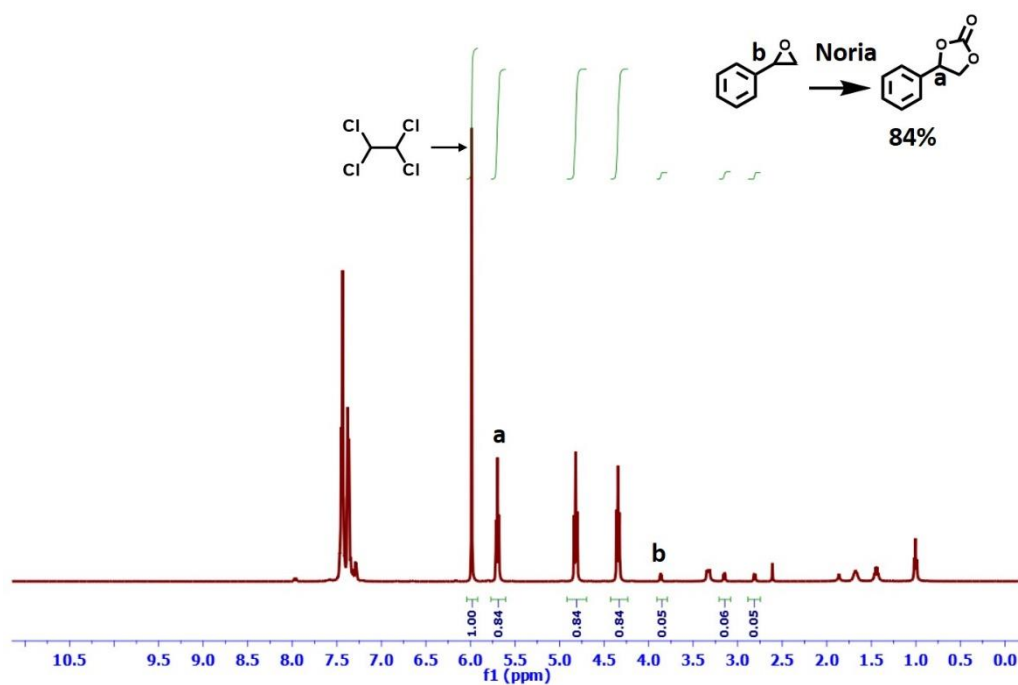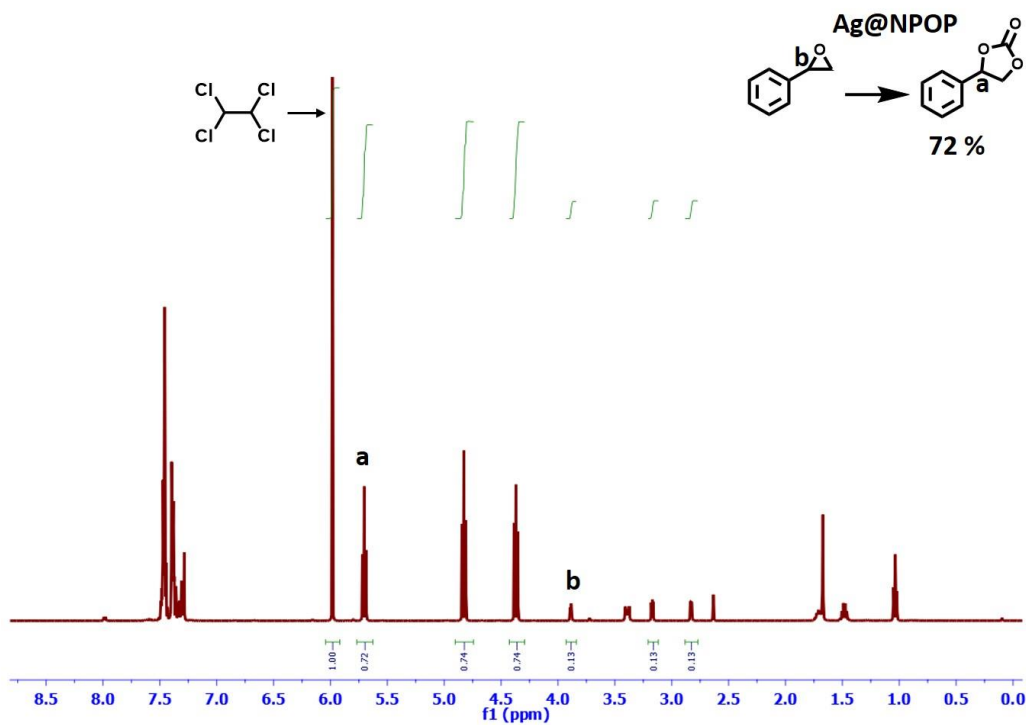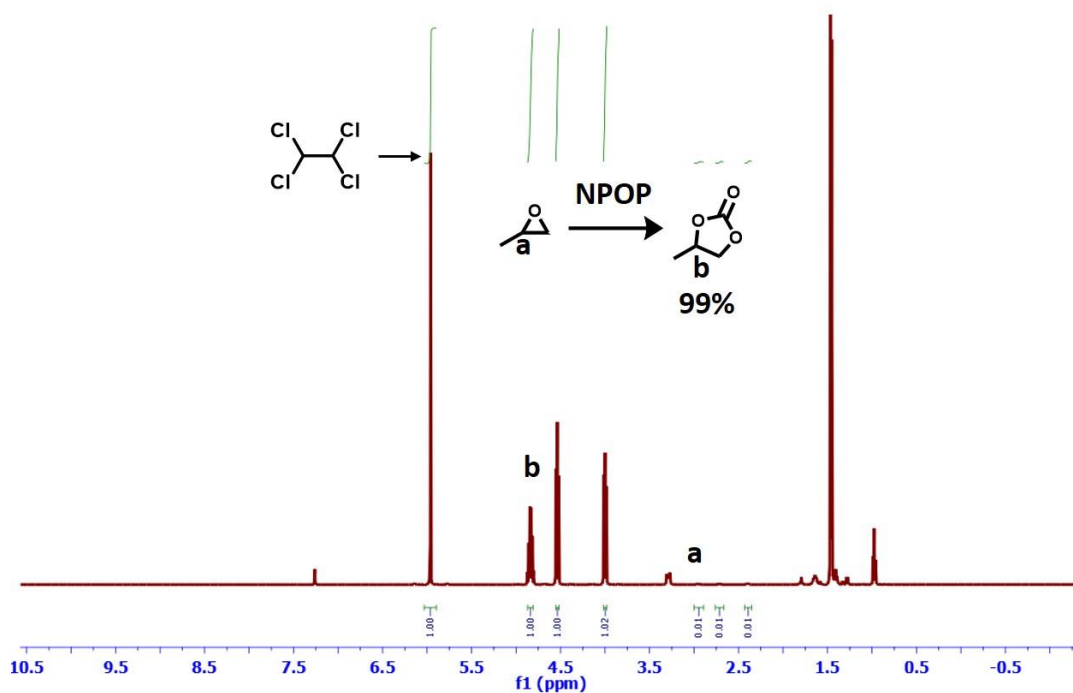
Fig. S30 ^{1}H NMR spectrum of the reaction mixture (in CDCl$_3$) for the conversion of styrene oxide with noria as a catalyst using 1,1,2,2-tetrachloroethane as external NMR standard.

Fig. S31 ^{1}H NMR spectrum of the reaction mixture (in CDCl$_3$) for the conversion of styrene oxide with Ag@NPOP as a catalyst using 1,1,2,2-tetrachloroethane as external NMR standard.

Fig. S32 ^{1}H NMR spectrum of the reaction mixture (in CDCl$_3$) for the conversion of propylene oxide with NPOP as a catalyst using 1,1,2,2-tetrachloroethane as external NMR standard.
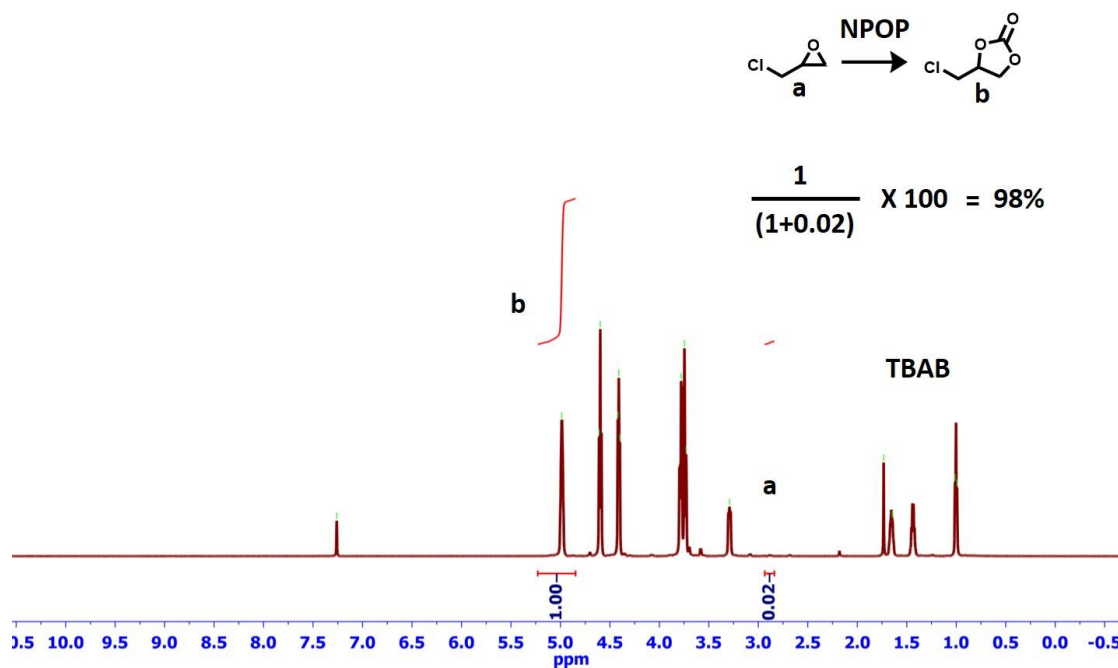

Fig. S33 ^{1}H NMR spectrum of the reaction mixture (in CDCl$_3$) for the conversion of epichlorohydrin with NPOP as a catalyst.
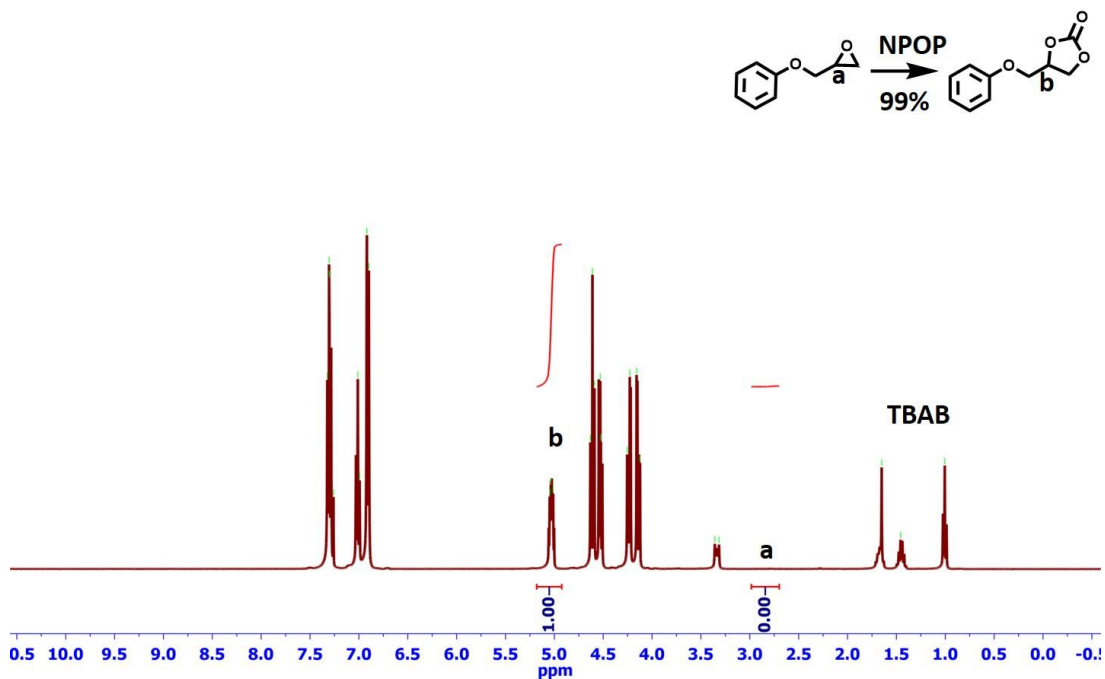
Fig. S34 ^{1}H NMR spectrum of the reaction mixture (in CDCl$_3$) for the conversion of 1,2-epoxy-3-phenoxypropane with NPOP as a catalyst.
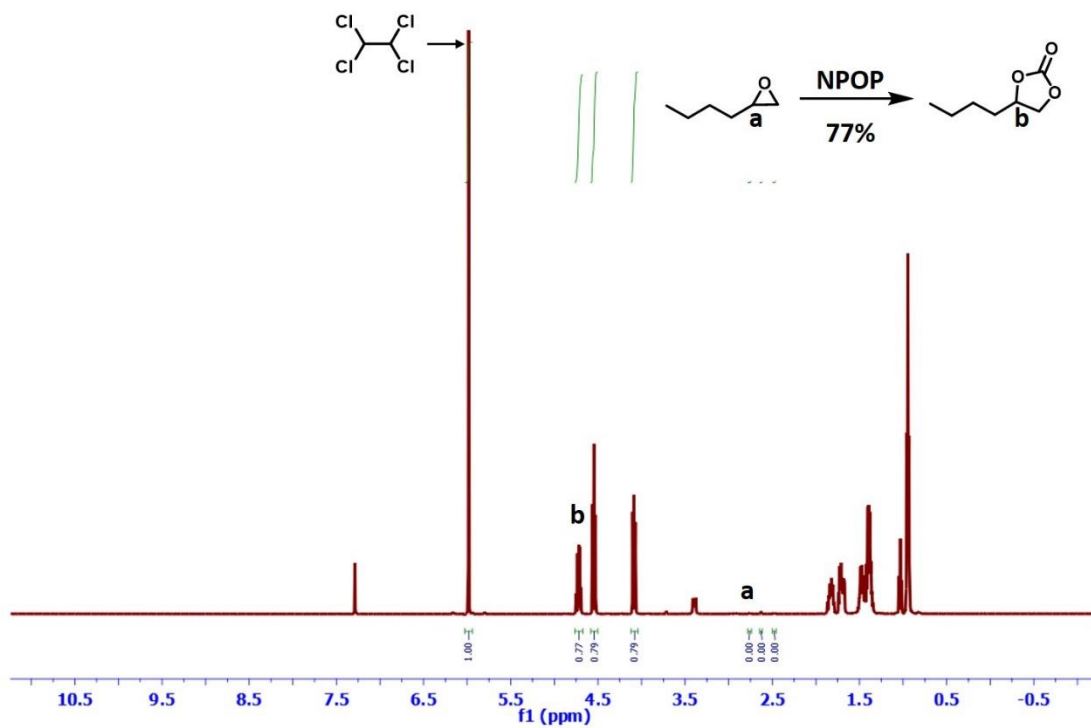

Fig. S35 ^{1}H NMR spectrum of the reaction mixture (in CDCl$_3$) for the conversion of 1,2-epoxyhexane with NPOP as a catalyst using 1,1,2,2-tetrachloroethane as external NMR standard.
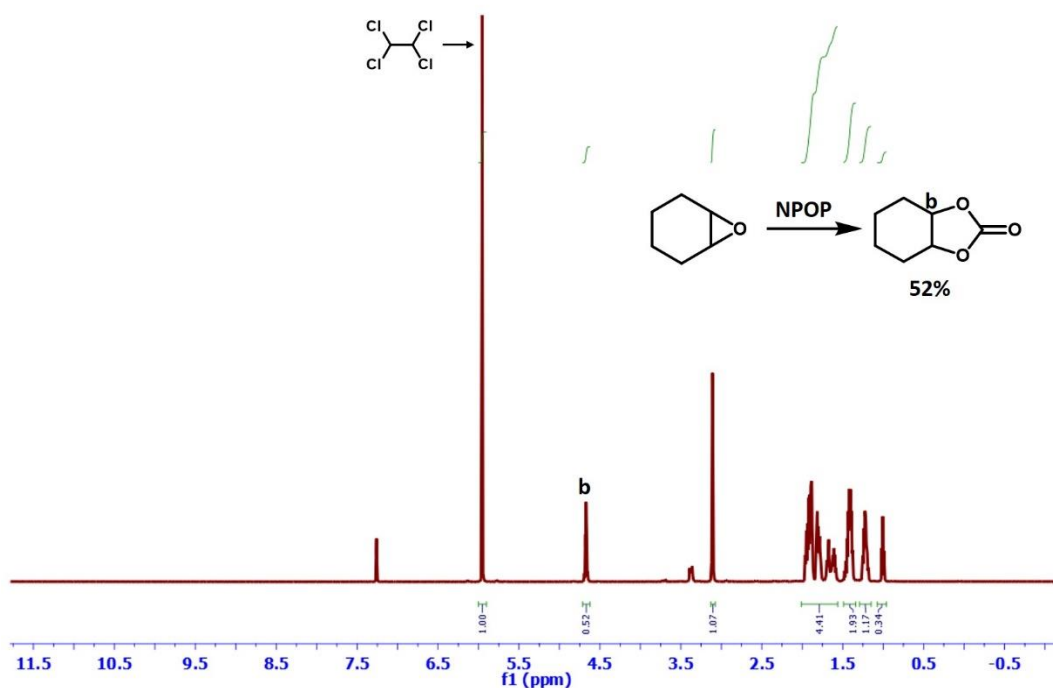
Fig. S36 ^{1}H NMR spectrum of the reaction mixture (in CDCl$_3$) for the conversion of cyclohexane oxide with NPOP as a catalyst using 1,1,2,2-tetrachloroethane as external NMR standard.
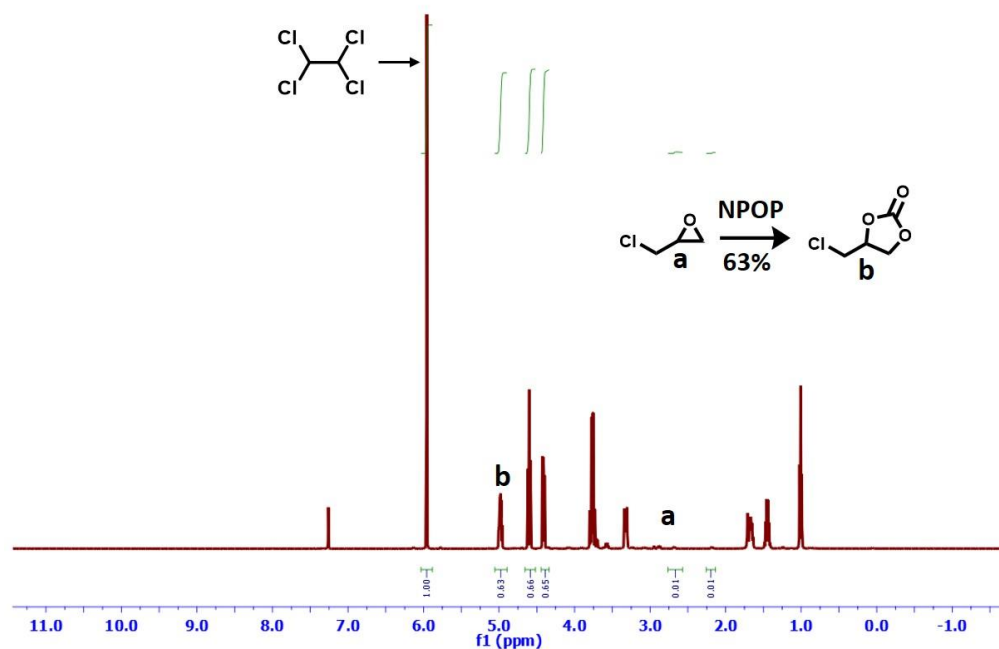

Fig. S37 ^{1}H NMR spectrum of the reaction mixture (in CDCl$_3$) for the conversion of epichlorohydrin with NPOP as the catalyst at 35°C, 1 bar CO$_2$ pressure, and for 24 h using 1,1,2,2-tetrachloroethane as external NMR standard.
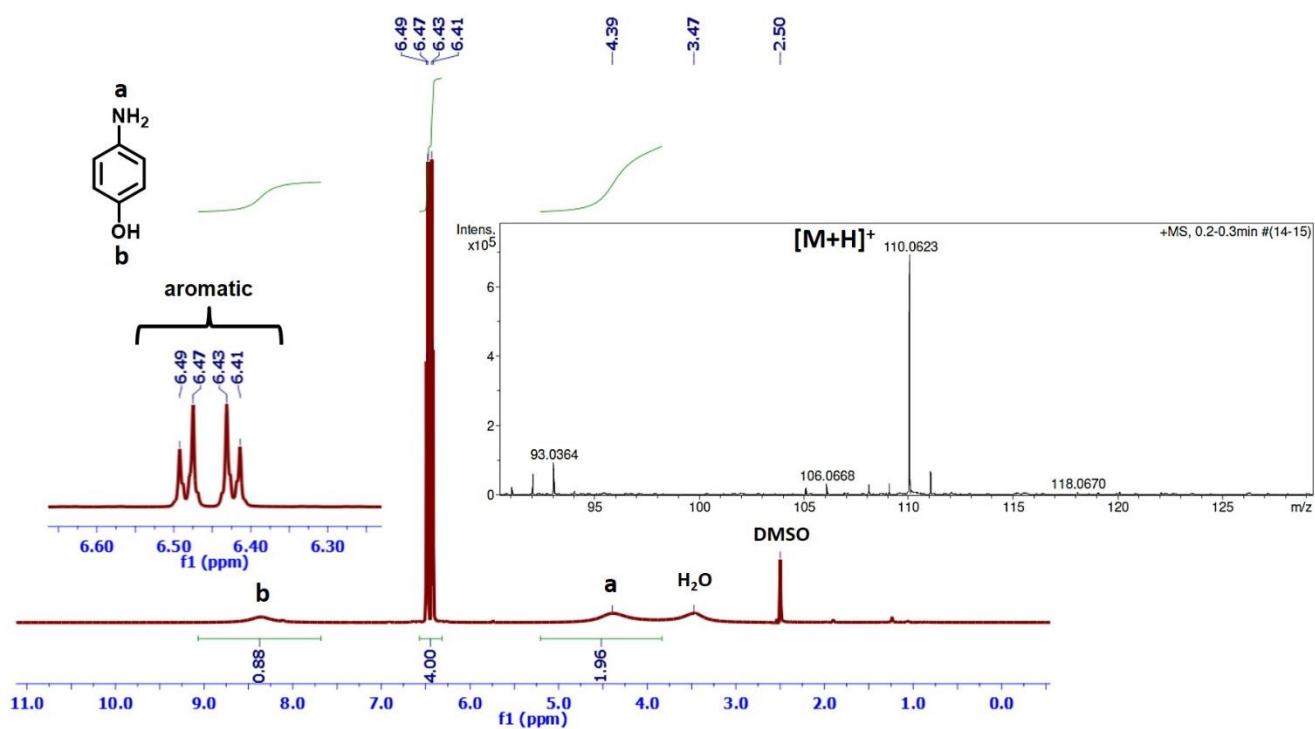
Fig. S38 ^{1}H NMR spectrum of the reaction mixture (in D$_6$-DMSO) for the conversion of *p*-nitrophenol (1 mmol) to *p*-aminophenol by Ag@NPOP as a catalyst (isolated yield: 90%; inset: HRMS analysis showing the molecular ion peak, [M+H]$^+$ at 110.0623).

Fig. S39 ^{1}H NMR spectrum of the reaction mixture (in CDCl$_3$) for the conversion of *o*-nitrotoluene (1 mmol) to *o*-aminotoluene by Ag@NPOP as a catalyst (isolated yield: 92%; inset: HRMS analysis showing molecular ion peak [M+H]$^+$ at 108.0831).

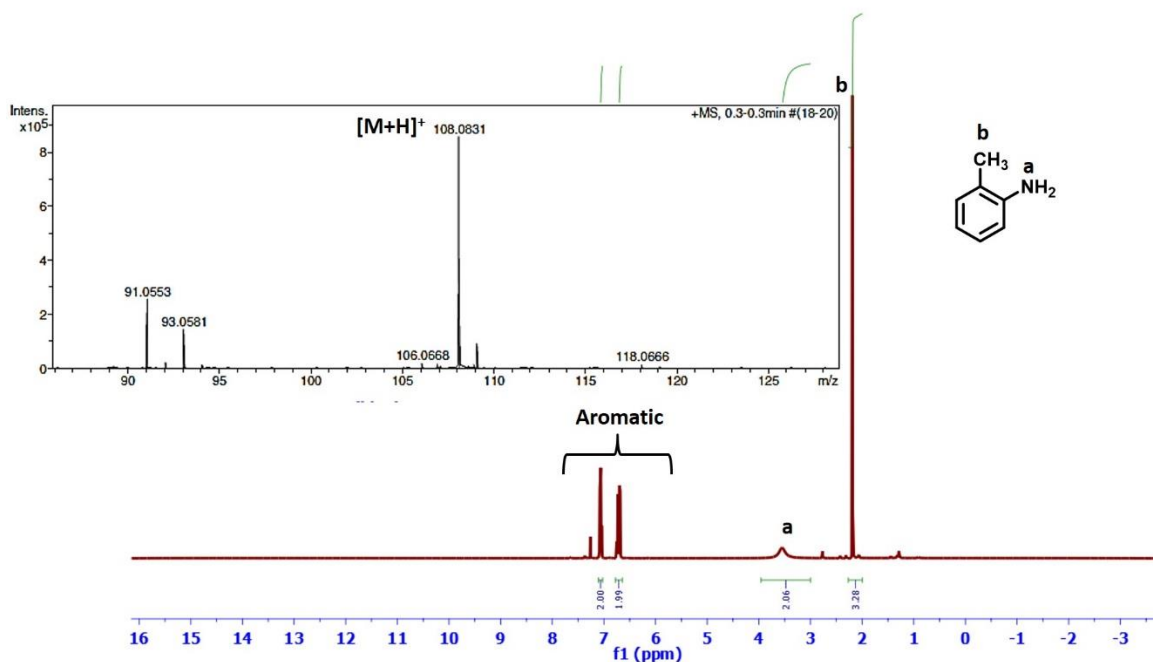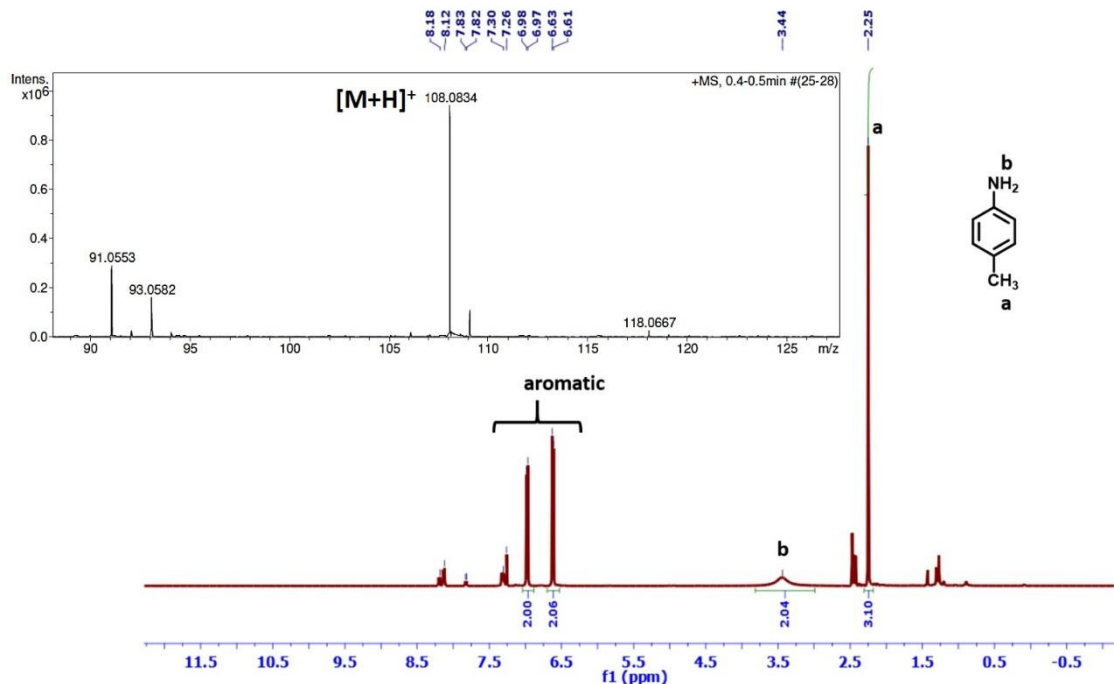**Fig. S40** ^{1}H NMR spectrum of the reaction mixture (in CDCl$_3$) for the conversion of *p*-nitrotoluene (1 mmol) to *p*-aminotoluene by Ag@NPOP as a catalyst (87 % conversion; inset: HRMS analysis showing the molecular ion peak, [M+H]$^+$ at 108.0834).
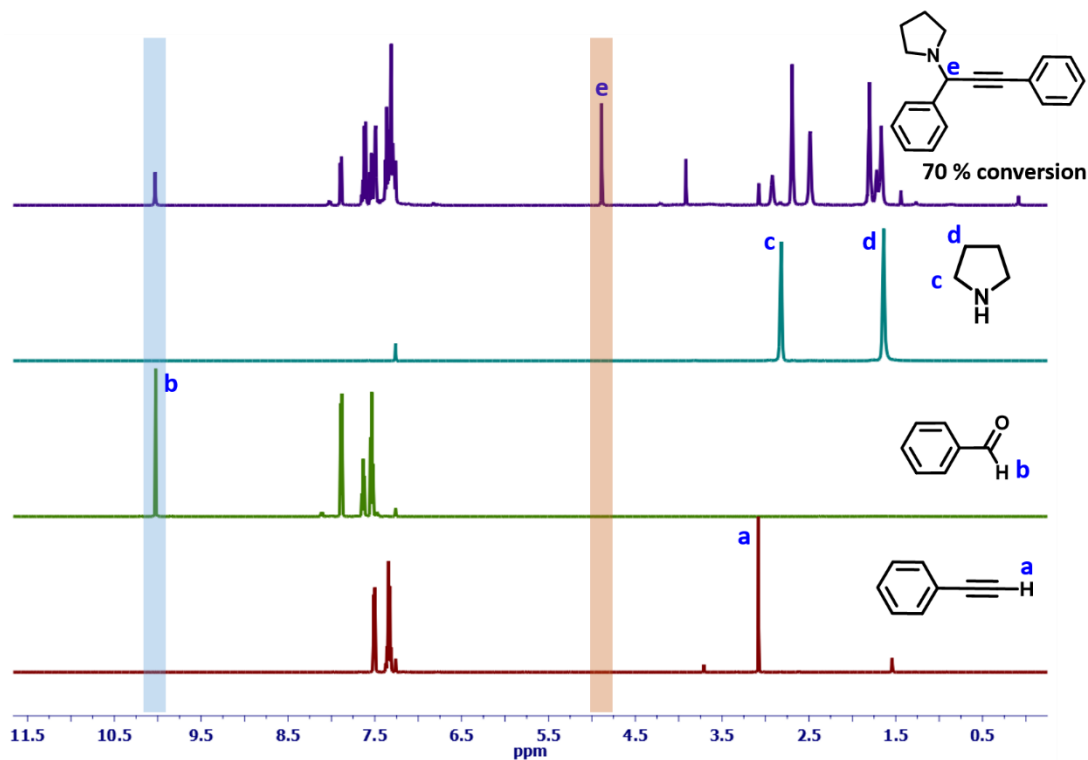

Fig. S41 A comparative ^{1}H NMR spectra (in CDCl$_3$) of the reaction mixture after removing THF, pyrrolidine, benzaldehyde, and phenylacetylene indicating the formation of propargylamine derivative. The % of conversion (70%) was estimated with respect to benzaldehyde.
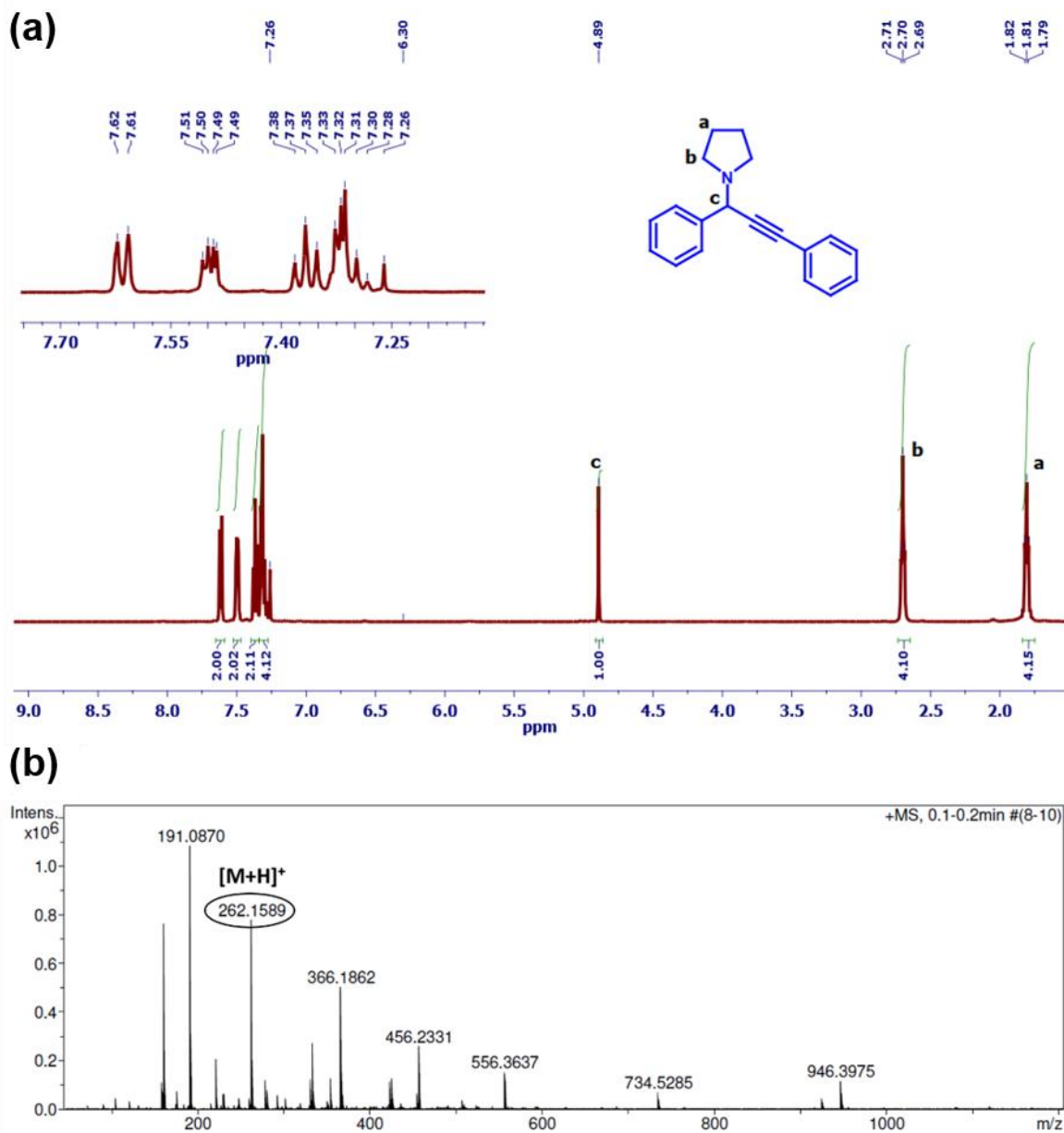
S38

Fig. S42 (a) ^{1}H NMR spectrum of 1-(1,3-diphenylprop-2-yn-1-yl)pyrrolidine after column purification (isolated yield: 68%). (b) HRMS data of the three-component coupling reaction mixture (in CHCl$_3$) catalyzed by Ag@NPOP suggesting the formation of the product ([M+H]$^+$: 262.1589).

Fig. S43 A comparative ^{1}H NMR spectra (in CDCl$_3$) of the reaction mixture after removing THF, pyrrolidine, 4-methoxybenzaldehyde and phenylacetylene indicating the formation of propargylamine derivative. The % of conversion (64%) was estimated with respect to 4-methoxybenzaldehyde.

Fig. S44 HRMS data of the three-component coupling reaction mixture (in CHCl$_3$) catalyzed by Ag@NPOP suggesting the formation of the product ([M+H]$^{+}$: 292.1694).
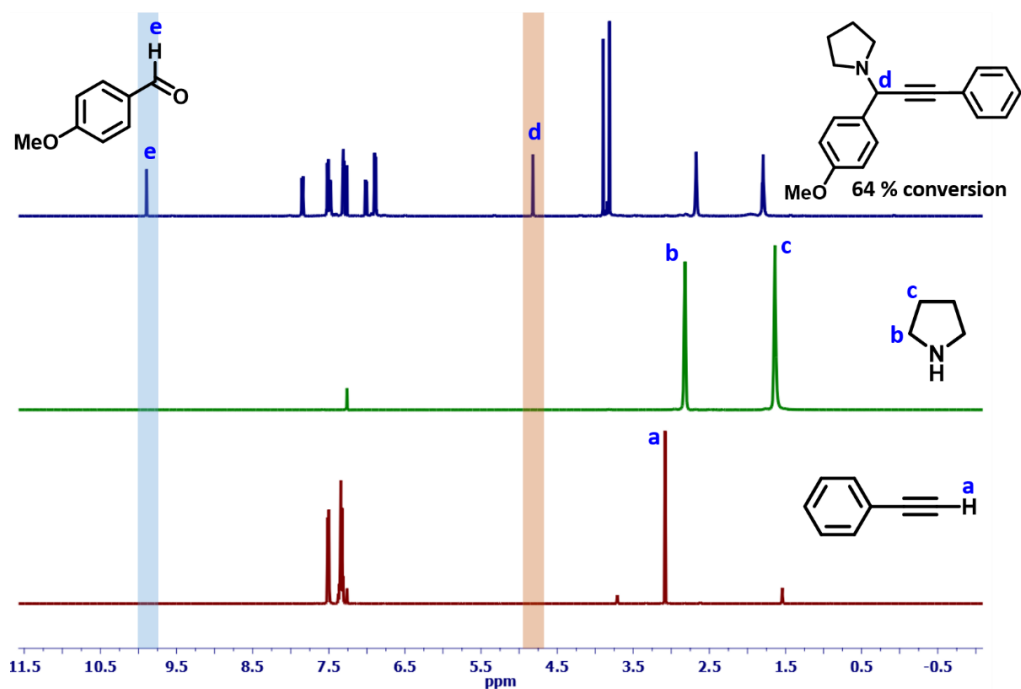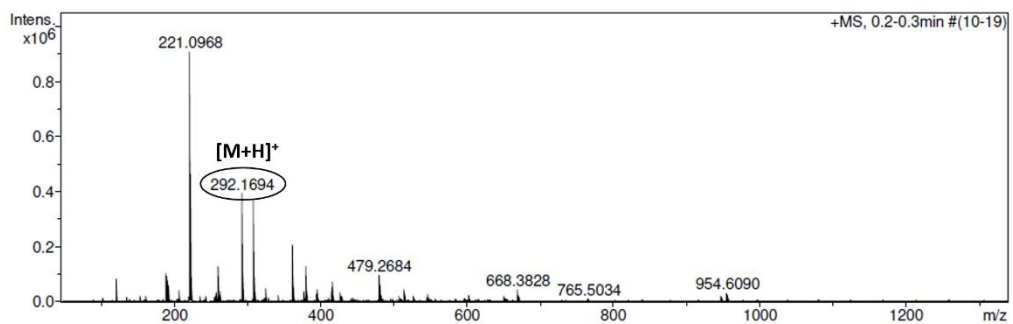
10. References

1. H. Kudo, R. Hayashi, K. Mitani, T. Yokozawa, N. C. Kasuga and T. Nishikubo, *Angew. Chem. Int. Ed.,* 2006, **45**, 7948.

2. A. Giri, A. Sahoo, T. K. Dutta and A. Patra, *ACS Omega*, 2020, **5**, 28413.

3. Y. Zhang, J. Duan, D. Ma, P. Li, S. Li, H. Li, J. Zhou, X. Ma, X. Feng and B. Wang, *Angew. Chem. Int. Ed.*, 2017, **56**, 16313.

4. A. Giri, M. W. Hussain, B. Sk and A. Patra, *Chem. Mater.,* 2019, **31**, 8440.

5. D. Shetty, S. Boutros, T. Skorjanc, B. Garai, Z. Asfari, J. Raya and A. Trabolsi, *J. Mater. Chem. A,* 2020, **8**, 13942.

6. H. Yang, Y. Du, S. Wan, G. D. Trahan, Y. Jin and W. Zhang, *Chem. Sci.,* 2015, **6**, 4049.

7. O. Buyukcakir, Y. Seo and A. Coskun, *Chem. Mater.*, 2015, **27**, 4149.

8. Z. Wang, H. Ma, T. Zhai, G. Cheng, Q. Xu, J. Liu, J. Yang, Q. Zhang, Q. Zhang, Y. Zheng, B. Tan and C. Zhang, *Adv. Sci.*, 2018, **5**, 1800141.

9. Q. Zhu, X. Wang, R. Clowes, P. Cui, L. Chen, M. A. Little and A. I. Cooper, *J. Am. Chem. Soc.*, 2020, **142**, 16842.

10. L. P. Skala, A. Yang, M. J. Klemes, L. Xiao and W. R. Dichtel, *J. Am. Chem. Soc.*, 2019, **141**, 13315.

11. M. Thommes, K. Kaneko, A. V. Neimark, J. P. Olivier, F. Rodriguez-Reinoso, J. Rouquerol and K. S. W. Sing, *Pure Appl. Chem.,* 2015, **87**, 1051.

12. J. X. Jiang, F. Su, A. Trewin, C. D. Wood, N. L. Campbell, H. Niu, C. Dickinson, A. Y. Ganin, M. J. Rosseinsky, Y. Z. Khimyak and A. I. Cooper, *Angew. Chem. Int. Ed.*, 2007, **46**, 8574.

13. M. W. Hussain, S. Bandyopadhyay and A. Patra, *Chem. Commun.*, 2017, **53**, 10576.

14. M. Alves, R. Mereau, B. Grignard, C. Detrembleur, C. Jerome and T. Tassaing, *RSC Adv.,* 2016, **6**, 36327.

15. Y. Yang, H. Ji, H. Duan, Y. Fu, S. Xia and C. Lü, *Polym. Chem.*, 2019, **10**, 4537.

16. A. K. Awasthi, S. D. Bhagat, R. Ramakrishnan and A. Srivastava, *Chem. Eur. J.*, 2019, **25**,12905.

17. M. E. Bosch, A. J. R. Sánchez, F. S. Rojas and C. B. Ojeda, *J. Pharm. Biomed. Anal.*, 2006, **42**, 291

18. T. Aditya, A. Pal and T. Pal, *Chem. Commun.*, 2015, **51**, 9410.

19. K. Sarmah, J. Pal, T. K. Maji and S. Pratihar*, ACS Sustainable Chem. Eng.*, 2017, **5**, 11504.

20. J. Strachan, C. Barnett, A. F. Masters and T. Maschmeyer, *ACS Catal.*, 2020, **10**, 5516.

21. W. Yan, R. Wang, Z. Xu, J. Xu, L. Lin, Z. Shen and Y. Zhou, *J. Mol. Catal. A: Chem.*, 2006, **255**, 81.

22. S. Wang, X. He, L. Song and Z. Wang, *Synlett*, 2009, 447.

23. X. Dong, Z. Gao, K. Yang, W. Zhang, L. Xu, *Catal. Sci. Technol.*, 2015, **5**, 2554.

24. S. J. Borah and D. K. Das, *Catal. Lett.*, 2016, **146**, 656.

25. D. Kim, H. Kim and J. Y. Chang, *Small*, 2020, **16**, 1907555.

26. Y. Yang, X. Zou, P. Cui, Y. Zhou, S. Zhao, L. Wang, Y. Yuan and G. Zhu, *ACS Appl. Mater. Interfaces*, 2017, **9**, 30958.

27. H. Li, B. Meng, S. H. Chai, H. Liu and S. Dai, *Chem. Sci.,* 2016, **7**, 905.

28. Y. Zhang, K. Su, Z. Hong, Z. Han and D. Yuan, *Ind. Eng. Chem. Res.,* 2020, **59**, 7247.

29. S. Lan, X. Yang, K. Shi, R. Fan and D. Ma, *ChemCatChem*, 2019, **11**, 2864.

30. H. Zhu, B. Shi, L. Gao, Y. Liu, P. R. Liu, L. Shangguan, Z. Mao and F. Huang, *Polym. Chem.*, 2017, **8**, 7108.

31. J. Rintjema, R. Epping, G. Fiorani, E. Martín, E. C. Escudero-Adán and A. W. Kleij, *Angew. Chem. Int. Ed.*, 2016, **55**, 3972.

32. S. Sopeña, E. Martin, E. C. Escudero-Adán and A. W. Kleij, *ACS Catal.*, 2017, **7**, 3532.

33. C. Miceli, J. Rintjema, E. Martin, E. C. E. Adán, C. Zonta, G. Licini and A. W. Kleij, *ACS Catal.* 2017, **7**, 2367.

34. V. Saptal, D. B. Shinde, R. Banerjee and B. M. Bhanage, *Catal. Sci. Technol.*, 2016, **6**, 6152.

35. Y. Zhi, P. Shao, X. Feng, H. Xia, Y. Zhang, Z. Shi, Y. Mu and X. Liu, *J. Mater. Chem. A*, 2018, **6**, 374.

36. P. Das and S. K. Mandal, *Chem. Mater.*, 2019, **31**, 1584.

37. Y. Zhao, Y. Zhao, J. Qiu, Z. Li, H. Wang and J. Wang, ACS *Sustainable Chem. Eng.*, 2020, **8**, 18413.

38. W. Zhou, Q. W. Deng, G. Q. Ren, L. Sun, L. Yang, Y. M. Li, D. Zhai, Y. H. Zhou and W. Q. Deng, *Nat. Commun.*, 2020, **11**, 4481.

39. D. Kim, D. W. Kim, O. Buyukcakir, M. Kim, K. Polychronopoulou and A. Coskun, *Adv. Funct. Mater.*, 2017, **27**, 1700706.

40. P. Li, X. Wang, J. Liu, H. S. Phang, Y. Li and Y. Zhao, *Chem. Mater.*, 2017, **29**, 9256.

41. P. Y. Wu, Y. Li, J. J. Zheng, N. Hosono, K. Otake, J. Wang, Y. H. Liu, L. L. Xia, M. Jiang, S. Sakaki and S. Kitagawa, *Nat. Commun.*, 2019, **10**, 4362.

42. K. Cho, S. M. Lee, H. J. Kim, Y. Ko, E. J. Kang and S. U. Son, *Chem. Eur. J.*, 2020, **26**, 788.

43. X. Wang, Y. Zhou, Z. Guo, G. Chen, J. Li, Y. Shi, Y. Liu and J. Wang, *Chem. Sci.*, 2015, **6**, 6916.

44. S. M. Sadeghzadeh, *Green Chem.*, 2015, **17**, 3059.

45. C. K. Ng, R. W. Toh, T. T. Lin, H. Luo, T. S. A. Hor and J. Wu, *Chem. Sci.*, 2019, **10**, 1549.

46. MD. W. Hussain, A. Giri and A. Patra, *Sustainable Energy Fuels*, 2019, **3**, 2567.

47. Y. Xie, T. T. Wang, X. H. Liu, K. Zou and W.Q. Deng, *Nat. Commun.*, 2013, **4**, 1960.

48. G. Ji, Z. Yang, H. Zhang, Y. Zhao, B. Yu, Z. Ma and Z. Liu, *Angew. Chem. Int. Ed.*, 2016, **55**, 9685.

49. F. Liu, K. Huang, Q. Wu and S. Dai, *Adv. Mater.*, 2017, **29**, 1700445.

50. MD. W. Hussain, V. Bhardwaj, A. Giri, A. Chande and A. Patra, *Chem. Mater.*, 2019, **31**, 8440.

51. S. N. Talapaneni, O. Buyukcakir, S. H. Je, S. Srinivasan, Y. Seo, K. Polychronopoulou and A. Coskun, *Chem. Mater.*, 2015, **27**, 6818.

52. D. Ma, J. Li, K. Liu, B. Li, C. Li and Z. Shi, *Green Chem.*, 2018, **20**, 5285.

53. S. Subramanian, J. Oppenheim, D. Kim, T. S. Nguyen, W. M. H. Silo, B. Kim, W. A. Goddard and C. T. Yavuz, *Chem*, 2019, **5**, 3232.

54. C. Cui, R. Sa, Z. Hong, H. Zhong and R. Wang, *ChemSusChem*, 2020, **13**, 180.

55. P. Pachfule, S. Kandambeth, D. D. Díaz and R. Banerjee, *Chem. Commun.*, 2014, **50**, 3169.

56. X. Shi, Y. Yao, Y. Xu, K. Liu, G. Zhu, L. Chi and G. Lu, *ACS Appl. Mater. Interfaces* 2017, **9**, 7481.

57. S. Lu, Y. Hu, S. Wan, R. McCaffrey, Y. Jin, H. Gu and W. Zhang, *J. Am. Chem. Soc.,* 2017, **139**, 17082.

58. Y. Zhu, W. D. Wang, X. Sun, M. Fan, X. Hu and Z. Dong, *ACS Appl. Mater. Interfaces* 2020, **12**, 7285.

59. R. Tao, X. Shen, Y. Hu, K. Kang, Y. Zheng, S. Luo, S.Yang, W. Li, S. Lu, Y. Jin, L. Qiu and W. Zhang, *Small*, 2020, **16**, 1906005.

60. Y. Su, X. Li, Y. Wang, H. Zhong and R. Wang, *Dalton Trans.,* 2016, **45**, 16896.

61. H. L. Cao, H. B. Huang, Z. Chen, B. Karadeniz, J. Lü and R. Cao, *ACS Appl. Mater. Interfaces*, 2017, **9**, 5231.

62. W. Gong, Q. Wu, G. Jiang and G. Li, *J. Mater. Chem. A*, 2019, **7**, 13449.

63. X. Q. Wu, J. Zhao, Y. P. Wu, W. Dong, D. S. Li, J. R. Li and Q. Zhang, *ACS Appl. Mater. Interfaces* 2018, **10**, 12740.

64. S. Goswami, H. Noh, L. R. Redfern, K. Otake, C. W. Kung, Y. Cui, K. W. Chapman, O. K. Farha and J. T. Hupp, *Chem. Mater.,* 2019, **31**, 1485.

65. Y. Yun, H. Sheng, K. Bao, L. Xu, Y. Zhang, D. Astruc and M. Zhu, *J. Am. Chem. Soc.,* 2020, **142**, 9, 4126.

66. N. Sun, C. Wang, H. Wang, L. Yang, P. Jin, W. Zhang and J. Jiang, *Angew. Chem. Int. Ed.*, 2019, **58**, 18011.

67. X. Yang, J. K. Sun, M. Kitta, H. Pang and Q. Xu, *Nat. Catal.*, 2018, **1**, 214.

68. Q. T. Fu, X. Yan, X. Y. Zhang, Y. He, W. D. Zhang, Y. Liu, Y. Li and Z. G. Gu, *Dalton Trans.,* 2020, **49**, 12145.

69. S. Cao, J. Chang, L. Fang and L. Wu, *Chem. Mater.,* 2016, **28**, 5596.

70. K. Sarmah, J. Pal, T. K. Maji and S. Pratihar, *ACS Sustainable Chem. Eng.* 2017*,* **5**, 11504.

71. Y. Song, H. Jiang, B. Wang, Y. Kong and J. Chen, *ACS Appl. Mater. Interfaces,* 2018, **10**, 1792.

72. C. Du, Y. Bai, Y. Shui, Y. Zhao, X. Zheng, S. Guo, Q. Wang, T. Yang, S. Wang, W. Dong and L. Wang, *ACS Appl. Nano Mater.*, 2019, **2**, 879.